MULTIPHASE CFD ANALYSIS OF DIRECT CONTACT CONDENSATION FLOW REGIMES IN A LARGE WATER POOL

A Thesis

by

Tyler Dee Hughes

Submitted to the Office of Graduate and Professional Studies of
Texas A&M University
In partial fulfillment of the requirements for the degree of

MASTER OF SCIENCE

Chair of Committee,	Karen Vierow Kirkland
Committee Members,	Debjyoti Banerjee
	Mark Kimber
Head of Department,	John Hurtado

August 2019

Major: Nuclear Engineering

ABSTRACT

This work considers the Pressure Suppression Chamber, a component of the Reactor Core Isolation Cooling System that is instrumental in maintaining core cooling capabilities during conditions such as the station blackout that occurred at Fukushima Daiichi. In previous experimental work at the NHTS Suppression Chamber facility, bulk pool temperature stratification was assessed during long term transients consistent with conditions at Fukushima. In this work, short-term mixing behavior in a BWR Suppression Chamber system is assessed using computational fluid dynamics.

In this work, direct contact condensation was modeled within STAR-CCM+ utilizing experimental conditions from Test Case #4 at the NHTS Suppression Chamber experimental facility. The Eulerian multiphase segregated flow model with the 2D axisymmetric formulation was employed. The steam-water condensation interaction was modelled utilizing the Hughes-Duffey Nusselt number correlation. The phase interface saturation temperature was treated as variable and was computed through the use of built in IAPWS steam tables within STAR-CCM+. Simulations were completed for an initial steam bubble formation and deformation phase within the Suppression Pool, accounting for a 48 ms overall transient.

It was found that the dynamics of steam bubble formation and deformation process most closely mirrors the bubbling direct contact condensation flow regime which was observed experimentally at the simulation initial conditions. However, the reason for the presence of this flow regime in the simulation was found to be attributable to an insufficient rate of condensation with the achieved condensation rate of 45.3 g/s only slightly exceeding the inlet steam mass flow rate to the Sparger of 45 g/s. The formation of a hot spot near the Suppression Chamber Sparger

outlet likely caused this flow regime to be observed experimentally. This led to the conclusion that better spatial resolution of the water temperature obtained from thermocouples near the Sparger outlet at the NHTS Suppression Pool facility would allow for a more realistic setting of initial conditions for future simulations of this kind. Also, based on the rapid pressure changes observed from the simulation presented in this work, an increase in measurement frequency of pressure instrumentation to at least 500 Hz was also recommended.

DEDICATION

This thesis is dedicated to my family. Your support has allowed me to pursue my academic goals and your continued support is instrumental as I continue to follow my passions in the next chapters of my life.

ACKNOWLEDGMENTS

I want to express my sincere gratitude to Dr. Karen Kirkland for her guidance and support throughout my research. Thank you for helping me realize my dreams of furthering my education.

I also extend my warmest regards to the U.S. Department of Energy Integrated University Program for the generous support provided by through the DOE IUP Graduate Fellowship program.

CONTRIBUTORS AND FUNDING SOURCES

Contributors

This work was supervised by a thesis committee consisting of Professor Karen Kirkland [advisor] and Professor Mark Kimber of the Department of Nuclear Engineering and Professor Debyoti Banerjee of the Department of Mechanical Engineering.

All work for the thesis (or) dissertation was completed independently by the student

Funding Sources

This material is based upon work financially supported under an Integrated University Program Graduate Fellowship. Any opinions, findings, conclusions or recommendations expressed in this publication are those of the author and do not necessarily reflect the views of the Department of Energy Office of Nuclear Energy.

TABLE OF CONTENTS

Page

LIST OF FIGURES

Page

LIST OF TABLES

Page

1. INTRODUCTION

Since the severe accident at Fukushima Daiichi, there has been a significant emphasis placed on understanding the progression of severe accidents initiated by a station blackout (SBO) scenario. In particular, this motivation has led to a focus on the Reactor Core Isolation Cooling (RCIC) system, a safety system in many currently operating Boiling Water Reactor (BWR) plants. The primary function of the RCIC system is to provide core cooling functions in the event that the main steam line becomes isolated from the plant turbine-generator, a condition consistent with the loss of offsite power that is characteristic of the early stages of a SBO.

After the accident at Fukushima, the RCIC system was identified as a key component in understanding the evolution of the accident due to its apparent ability to operate beyond its current design basis operating limits. According to Gauntt at Sandia National Laboratories, the RCIC system is typically credited for between 4 to 8 hours of operating time in probabilistic risk assessment (PRA) studies and BWR plant design basis documents [1]. However, at Fukushima the RCIC system operated at Units 2 and 3 for 72 and 21 hours respectively before reaching a shutdown condition upon which core uncovery and subsequent melting began [1].

The extended operating time of the RCIC system, even under off-normal operating conditions, has led to the realization that the RCIC system is more robust than anticipated [1]. Thus, current research is aimed at gaining further insight into the physical mechanisms that drive the primary components of the system, with the goals of:

- Providing this insight to plant owners who could potentially use this improved understanding to justify crediting this this system for longer durations in risk assessments and plant procedures.
- Informing the development of new computational models of RCIC system components capable of being used in systems level modelling codes that can simulate complete plant operating transients under conditions like those at Fukushima Daiichi.

1.1 Statement of Purpose

The purpose of the proposed research is to examine the Pressure Suppression Chamber, a component of the RCIC system that contains complex multiphase flow behavior. Past research into the Pressure Suppression Chamber focused on its long-term performance with the goal of assessing temperature stratification that can occur in the system and lead to inoperability of the RCIC system pump. In this thesis, small time scale thermal hydraulic phenomena including direct contact condensation flow regimes are considered.

1.2 Technical Approach

In the past, the creation of new physical models for components of the RCIC system has been approached computationally using computational fluid dynamics (CFD). Using CFD, the physical processes governing RCIC system components are assessed at fine resolution, giving insight into the physical phenomena that are most important to capture within analytical models. When possible, experimental data has been used to validate the CFD models, ensuring that the physical processes are adequately being represented.

In the proposed research, the same process is implemented. Using a CFD model developed for the Nuclear Heat Transfer Systems (NHTS) experimental facility, direct contact condensation

in a steam-water system is captured along with the induced direct contact condensation flow regime. In particular, the chugging and bubbling direct contact condensation flow regime are considered due to their prevalence in NHTS experimental test cases. Available experimental data from the NHTS facility is used to apply appropriate initial and boundary conditions to the model.

1.3 Significance of Work

The goal of this modelling effort is to apply appropriate physical models within the framework of a commercial CFD software, STAR-CCM+, in order to capture the dynamics of a single bubble formation and collapse for a specific experimental test case at the NHTS facility. By capturing the steam-water flow dynamics and presence of condensation phenomena, the CFD model has applicability to future experimental work:

- Informing future experimental design changes at the NHTS Suppression Chamber facility including the addition of thermocouples and pressure sensors that will allow for the capability of CFD model validation.
- Validation that current NHTS Suppression Chamber facility support structures don't interfere with bubble formation and collapse dynamics.
- Informing experimentalist about flow behavior that may occur on time scales that are currently not captured by the data collection frequency of currently used instrumentation.

Development of the current model also has applicability to the understanding of direct contact condensation phenomena present in steam-water Suppression Chamber systems:

- The relationship between condensation rate and the observed direct contact condensation flow regime is shown.

- The dynamics of the initial bubble formation and deformation in a Suppression Pool are shown to be greatly influenced by significant changes in pressure as steam is expelled into the Pool.
- It is shown that a high degree of subcooling in the Suppression Pool leads to high enough condensation rates that significantly deform the steam bubble and prevent steam from rising towards the Suppression Pool surface. This prevents vertical temperature stratification during a long-term operating transient.
- Obtaining a higher resolution vertical water temperature profile from experimental tests is identified as essential for providing initial conditions in simulations that will translate to observing the correct direct contact condensation flow regimes.

2. BACKGROUND

In this section, the RCIC system is described in brief detail with an emphasis placed on one of its components, the Pressure Suppression Chamber, which is the focus of this research. Furthermore, this section provides a further description of the principal thermal-hydraulic phenomenon of interest in this research: direct contact condensation flow regimes.

2.1 RCIC System Component Overview

Figure 1 shows an overall component diagram of the RCIC system with relation to the reactor pressure vessel.

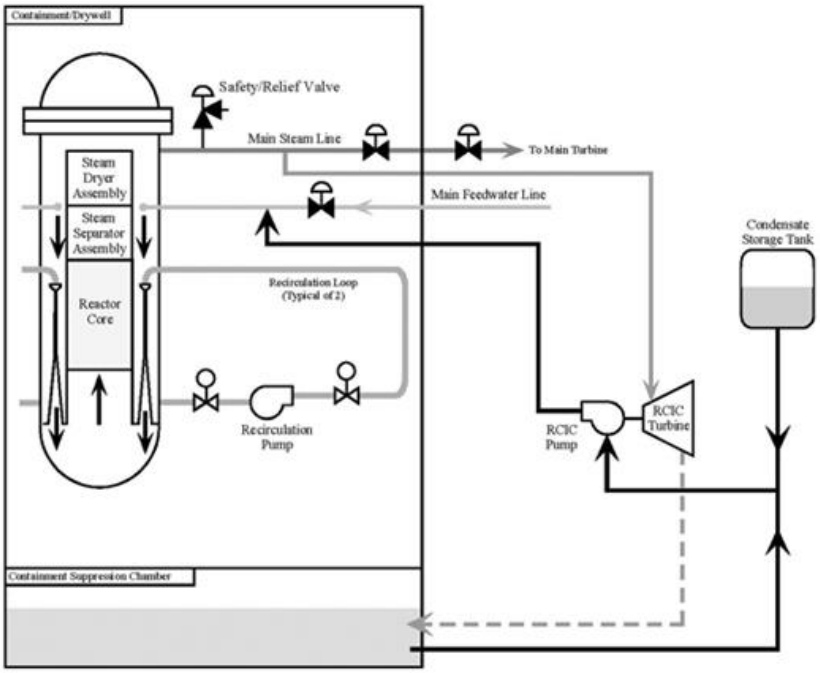

Figure 1. RCIC System Component Diagram with Relation to Core Cooling Functionality [2]

Overall, the RCIC system is composed of three primary components listed as follows:

1. Multi-stage turbine-driven centrifugal pump
2. Terry Turbine
3. Pressure Suppression Chamber

These components operating together utilize steam flow exiting the reactor core to drive the introduction of cooling water to the reactor core for the purpose of decay heat removal post reactor SCRAM.

Steam from the reactor core is diverted from the main steam line to the Terry Turbine. This impulse type turbine utilizes the enthalpy of incoming steam to generate kinetic energy for the turbine rotor which spins a shaft that connects the Terry Turbine to the RCIC Pump. The RCIC Pump, utilizing the generated shaft work, supplies cooling water from either the plant's condensate storage tank (CST) or the Pressure Suppression Chamber to the reactor pressure vessel (RPV). Finally, steam that has fully expanded within the Terry Turbine is exhausted into the Pressure Suppression Chamber, a vessel of water which serves as the ultimate heat sink for the RCIC system alongside its role as a secondary source of cooling water supply to the RCIC Pump.

2.2 Normal and Off-Normal Conditions of RCIC Performance

As previously explained, the RCIC system begins operation when the main steam line is isolated from the primary plant turbine. This condition can occur for various reasons [3]:

- Loss of Offsite and Onsite AC Power: AC power needed to operate primary plant systems leads to necessary shutdown of the primary plant turbine.

- Loss of feedwater flow: Feedwater flow that is normally supplied to the RPV through the primary plant condensate pump is lost leading to a necessary reactor SCRAM and shutdown of the primary plant turbine.

In the context of Fukushima, the loss AC power condition is most relevant. With the loss of AC power, the RCIC system is initiated. The RCIC system requires DC power to operate certain components within the system including the Terry Turbine governor valve, therefore DC power is supplied from batteries that are located at the plant site [4]. Ultimately, as long as DC power is available onsite, the RCIC system is capable of controlling steam flow into the Terry Turbine by actuation of the governor valve. The diverted steam flow provides the energy needed to produce the operating torque for the Terry Turbine and RCIC Pump shaft, and this allows for maintenance of the RPV water level for core cooling.

Under this normal operating condition, the RCIC system is credited in plant safety analyses for between 4-8 hours of continuous operation. Beyond this operating time, it is assumed that the onsite DC power supplies will be depleted leading to loss of electronic flow control for the RCIC system [4].

However, at Fukushima the RCIC system was observed to operate well beyond this plant design basis limit. Without DC power for steam flow control to the Terry Turbine, it is evident that the RCIC system is capable of sustaining a self-regulating mode where the Turbine is able to operate even under possible two-phase flow conditions.

2.3 Pressure Suppression Chamber Description

The Pressure Suppression Chamber, sometimes referred to as the wetwell, is typically located below the RPV in BWR Mark I containment structures as shown in Figure 2.

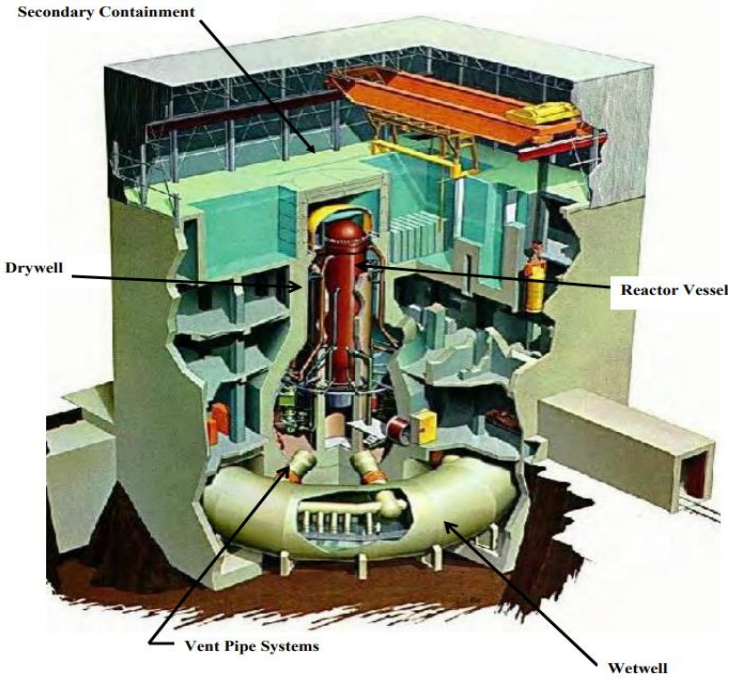

Figure 2. BWR Mark I Containment Design Diagram [5]

In this containment design, the drywell is a concrete structure which contains the RPV. The Pressure Suppression Chamber, located below the RPV, is a toroidal shaped tank which is typically filled to its midpoint with subcooled water [5]. The drywell and Pressure Suppression Chamber are connected through vent lines. In the event that steam enters the drywell, ambient pressure within the drywell can be reduced by venting to the vapor space of the Pressure Suppression Chamber as long as drywell pressure is sufficient to drive the flow [5].

Figure 3 shows a section diagram of the Pressure Suppression Chamber. To fulfill its purpose as the primary heat sink for the RCIC system, the Chamber consists of a steam Sparger line that enters the Chamber and is submerged within subcooled water. The Sparger can take upon different designs depending on the plant under consideration. In the simplest case, the Sparger is

a pipe with a single open-ended outlet. In other designs, the Sparger has multiple machined outlet holes located below the water level of the Chamber.

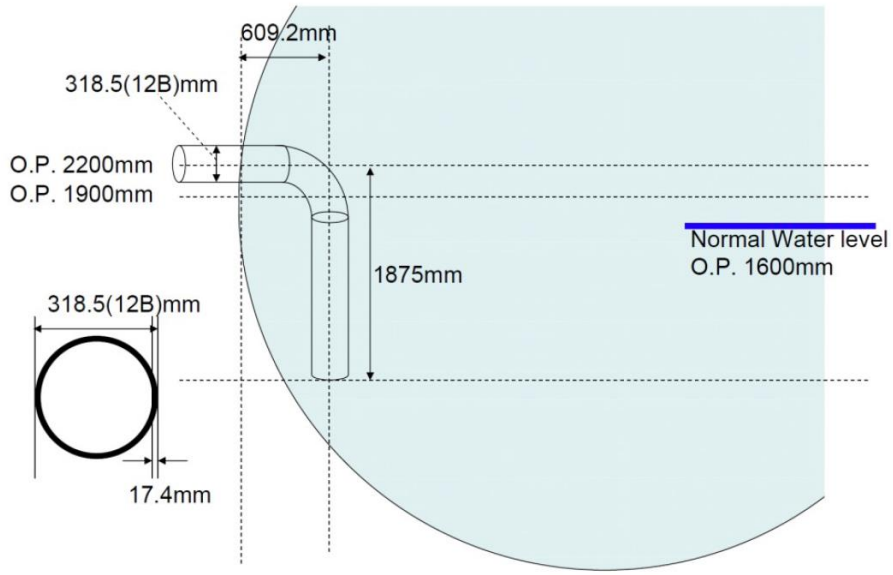

Figure 3. Fukushima Unit 2 Pressure Suppression Chamber Cross-Sectional Diagram [6]

The Pressure Suppression Chamber is also connected to a suction side of the RCIC Pump. The location of this suction line is likely to be dependent on individual plant design, but its location is integral to the long-term operation of the RCIC system [7].

One focus of recent Pressure Suppression Chamber research is the thermal stratification phenomenon. Thermal stratification occurs when steam injected into the water Chamber does not induce the necessary mixing needed to uniformly distribute heat within the Chamber. Therefore, if thermal stratification takes place, temperature gradients can be established in the Chamber leading to various operational difficulties.

One of these issues pertains to the capability of the Pressure Suppression Chamber to serve its capacity as a secondary cooling water source for the RCIC Pump. If the thermal stratification causes a localized warmer region of water near the suction line in the Pressure Suppression Chamber, the net positive suction head available to the RCIC Pump may be insufficient leading to failure of the Pressure Suppression Chamber to fulfill its function [7].

Another issue pertaining to the Pressure Suppression Chamber's responsibility to regulate drywell pressure. If thermal stratification takes place, the effectiveness of the heat transfer between the injected steam and subcooled water can degrade. Therefore, it is possible that incomplete condensation of injected steam could raise the vapor space pressure in the Chamber such that vapor flow between the drywell and wetwell is prevented [7].

2.4 Direct Contact Condensation Flow Regimes

With temperature stratification in the Chamber being a possible outcome when operating the RCIC system long term, it is imperative to understand the thermal hydraulic mechanisms that drive the mixing of water within the Chamber.

The degree of mixing local to the outlet of the Sparger is primarily dictated by the interaction between steam and water. In the Pressure Suppression Chamber, unlike typical heat exchanger devices with phases separated by a physical barrier, heat transfer takes place at an interface that is in direct contact. With the phases being in direct contact, mass transfer (condensation) takes place across the interface, and the rate of condensation is influenced by turbulent flow characteristics at the interface, the degree of subcooling in the water, and the rate of steam flow into the Sparger.

According to de With et al., direct contact condensation between steam and water is characterized by steam thermal hydraulic behavior [8]. Therefore, the behavior of steam in this type of interaction has been divided into direct contact condensation flow regimes. Important to the identification of a flow regime are two main parameters: the mass flux of the steam flow and the degree of subcooling in the water.

de With et al. compiled data from many experiments that examined flow behavior in a system consisting of a subcooled water tank containing a steam injector. These studies varied the inlet mass flux of steam to the injector along with the degree of water subcooling. Based on the resulting flow behavior in the experiments, de With et al. generated a three-dimensional direct contact condensation flow regime map. This regime map is shown in Figure 4.

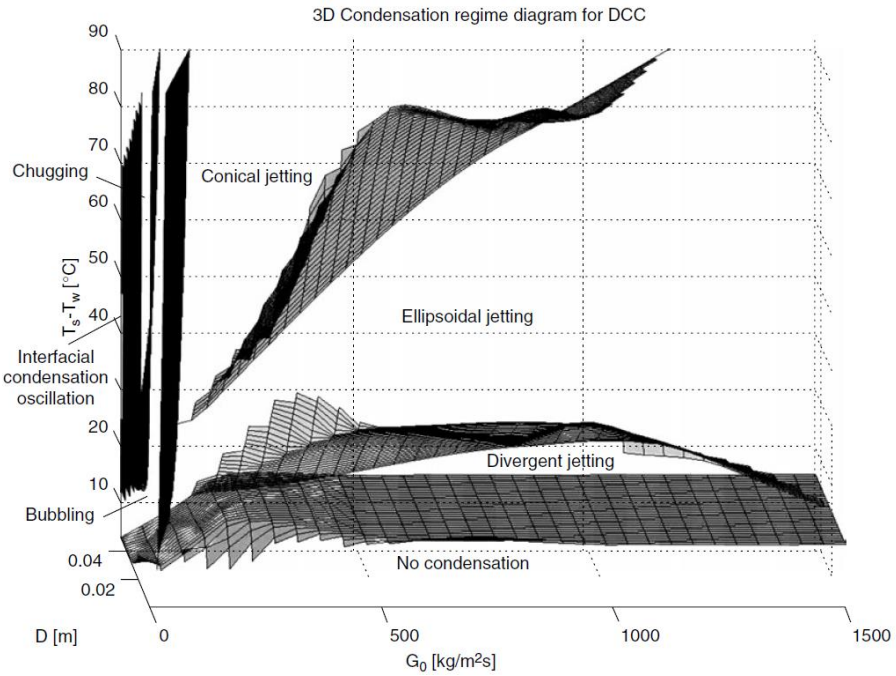

Figure 4. Direct Contact Condensation Regime Map [8]

As shown in Figure 4, three major direct contact condensation flow regimes were identified: chugging, bubbling, and jetting. While the inlet mass flux and degree of water subcooling are alone sufficient to generate a mapping of flow regimes, de With et al. also included the diameter of the steam injector as a third variable. This addition mainly highlights the fact that experimental studies on direct contact condensation have utilized a wide range of injector diameters leading to some differences in their own two-dimensional regime maps [8].

In Figure 4, the region of intermediate steam mass flux leads to the bubbling direct contact condensation flow regime. In the bubbling regime, steam exits the injector with inertial forces dictating the rate of bubble growth at the mouth of the injector. As the steam bubble grows in the subcooled water pool, the available interfacial area between steam and water increases leading to an increase in condensation occurring at the interface. Eventually, the growth of the bubble becomes primarily limited by condensation with the bubble eventually detaching from the injector due to instability induced by the increasing condensation rate.

In Figure 4, the region of high steam mass flux is called the jetting regime. In this regime, the inlet mass flux of steam is high enough such that a jet is formed in the water pool. de Wtih et al. identified different possible steam jet geometries depending on the subcooling in the pool [8]:

- Divergent Jet: Irregular shaped jet that occurs at low subcooling.
- Ellipsoidal Jet and Conical Jets: Jets with smooth steam-water interface occurring at intermediate to high subcooling

Finally, the last direct contact condensation flow regime is called chugging. This flow regime was prevalent in experiments performed at the NHTS facility due to the setup of low steam mass flux and high degrees of subcooling.

In the early stages of the chugging flow regime, the steam bubble growth behavior is similar to the bubbling regime. However, in the chugging regime, the steam bubble violently collapses at the injector outlet rather than slowly detaching. The collapse of the bubble occurs due to the condensation rate greatly exceeding the inlet steam mass flow rate causing a large amount of interfacial instability.

With the collapse of the steam bubble, a large pressure gradient is formed that causes water to flow back into the steam injector. The steam-water interface reforms in the injector, and the process can repeat as long as subcooling in the pool is sufficiently high to allow a high enough condensation rate.

The size of bubbles before detachment (or collapse) from the injector outlet is influenced by the degree of subcooling within the water pool. Recognizing the influence of subcooling on steam bubble size, Kerney et al. introduced a dimensionless parameter called the condensation potential as a variable to correlate with steam plume length as shown in Equation 2.1 [9].

$$B = \frac{c_p}{h_{fg}} (T_{sat} - T_w) \tag{2.1}$$

Experimental evidence supports the use of the condensation potential as a benchmark for steam plume length. Purhonen et al. performed steam-water suppression pool testing at the POOLEX facility where their use of high speed cameras confirms the intuitive role of pool subcooling on bubble size, assuming that the mass flux of steam is maintained in a tight interval [10].

3. LITERATURE REVIEW

In this section, a literature review is conducted to provide context to two of the prominent Pressure Suppression Chamber experimental facilities: NHTS and POOLEX. Next, current direct contact condensation CFD modelling techniques are examined in order to provide context to the approach used in developing a CFD model for the NHTS facility using conditions from experimental tests.

3.1 Current Suppression Chamber Experimental Facilities

In order to gain insight into Pressure Suppression Chamber thermal-hydraulic performance characteristics, experimental facilities have been constructed that are scaled representations of a true Pressure Suppression Chamber found at operating plants. Two well established Suppression Chamber experiments, NHTS and POOLEX, have provided significant insights relevant to this research.

3.1.1 NHTS Suppression Chamber Facility

The NHTS Suppression Pool Facility was designed by Matthew Solom at Texas A&M University. The primary goal of research performed at this facility was to examine the temperature stratification phenomenon over long operation times. Figure 5 shows a picture of the NHTS Suppression Chamber.

The NHTS Suppression Chamber has a horizontal orientation and is a fully enclosed vessel. The Suppression Chamber is connected to a steam generator which serves as a steam source analogous to the reactor pressure vessel [7]. The Suppression Chamber is also connected to a

centrifugal pump which performs the role of the RCIC Pump using the Suppression Chamber as a suction source [7].

Figure 5. NHTS Suppresion Chamber Experimental Facility [7]

The NHTS Suppression Chamber receives steam from the steam generator through a single open-ended Sparger line. The Suppression Chamber contains an internal support structure that allows for the placement of thermocouples at different locations within the Chamber. The Chamber itself does contain a vapor space at the top which can be pre-pressurized or vented to atmospheric pressure. Figure 6 shows a diagram of the Chamber internal instrumentation. Note that black dots in Figure 6 represent thermocouple locations along the Chamber vertical axis.

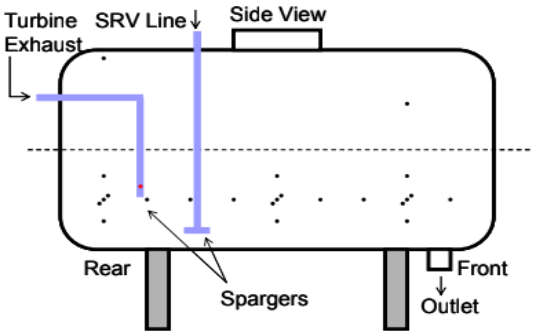

Figure 6. Internal diagram of NHTS Suppression Chamber [7]

At the NHTS Suppression Chamber facility, 32 experimental tests were run with varying steam generator power, vapor space pressurizations, and injection modes. Twenty-seven tests were performed using the regular Sparger. Five tests involved the use of the analog SRV line which is not considered in the proposed research.

Out of the 27 tests with the regular Sparger, three power levels were considered: 157 kW, 107 kW, and 57 kW [7]. With the steam generator operating at these powers, the Sparger inlet steam mass fluxes are: 50 kg m^{-2} s^{-1}, 34 kg m^{-2} s^{-1}, and 18 kg m^{-2} s^{-1} respectively [7]. At these inlet mass fluxes, the NHTS facility was clearly operating in the chugging direct contact condensation flow regime considering initial Pool subcooling. While the NHTS Suppression Pool facility does not provide visual contact with the internal space of the Chamber during the experiment, chugging was audibly observed early in many of the test cases [7].

Some tests were performed with the vapor space pre-pressurized and isolated from atmosphere. However, most test utilized a standard pressurization scheme that was initially vented to atmosphere. In the standard scheme, the Chamber was not vented throughout testing,

thus pressure in the vapor space increased over time which was found to induce a greater level of temperature stratification [7] [11].

After performing these tests, it was observed that temperature stratification was exhibited vertically within the Chamber to varying degrees in all tests utilizing the standard steam Sparger [7]. The onset of thermal stratification occurred at an accelerated pace once chugging weakened leading to decreased mixing within the Chamber characteristic of the bubbling flow regime [7]. Ultimately, without visualization methods, the primary evidence for the existence of chugging in these experiments came from differential pressure and temperature oscillations in the Sparger. The temperature oscillations indicated that water ingress into the Sparger indeed did occur with subcooled temperatures periodically observed within the Sparger [7].

3.1.2 Comparison of NHTS and POOLEX Suppression Chamber Facilities

The POOLEX Suppression Chamber experimental facility at Lappeenranta University of Technology in Finland was designed to examine a variety of Suppression Chamber thermal-hydraulic phenomena. Similarly to the NHTS facility, the POOLEX facility also performed temperature stratification experiments (referred to as STB-20 and STB-21). These experiments showed similar behavior to the NHTS experiments with chugging playing an integral role in maintaining mixing within the Chamber [12]. When steam mass flow rate was set low enough to allow full condensation within the Sparger, temperature stratification was substantial due to the lack of chugging acting as a source of momentum to drive mixing in the Chamber [12]. However, increasing the steam mass flow rate led to enhanced mixing that generated more temperature uniformity in the Chamber [12].

While the NHTS facility was developed to exclusively examine temperature stratification, a long-term operation phenomenon, the POOLEX facility was developed to also consider visualization of steam bubble formations within the Chamber. With the addition of high speed cameras and viewports within the Chamber, experiments considering direct contact condensation flow regime dynamics could be performed with the goal of providing data needed for computational model validation for steam injection into subcooled water [13]. Figure 7 shows a diagram of the overall POOLEX Suppression Chamber.

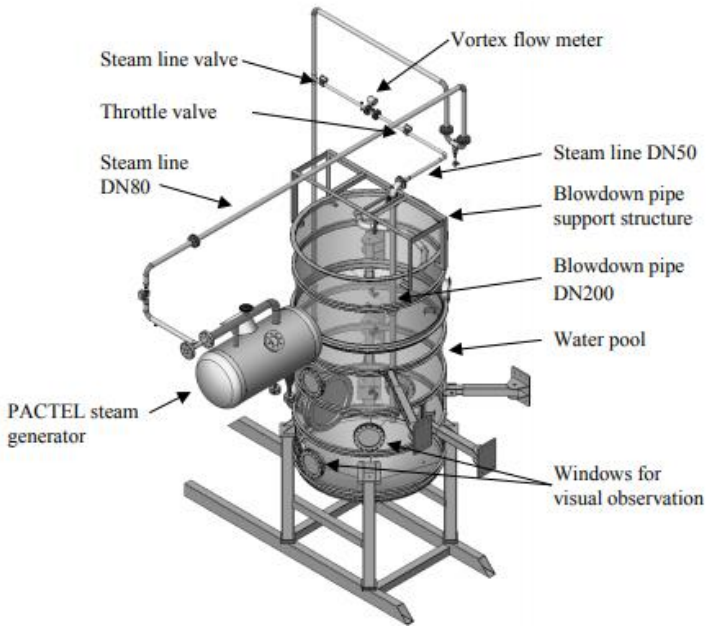

Figure 7. POOLEX Suppression Chamber Diagram [12]

Table 1 shows a geometric and operational comparison between the POOLEX and NHTS facilities. Note that the inlet steam mass flow rates were taken for two particular tests, one for each facility. The commonality between these tests is the exhibition of the chugging direct contact condensation flow regime.

Table 1. NHTS and POOLEX Experimental Facility Comparison [7] [10]

Design Parameters	POOLEX (STB 28-4 Test)	NHTS (Test Case #4)
Pool Orientation	Vertical	Horizontal
Sparger Diameter	21.91 cm	4.1 cm
Primary Axis Length	4.4 m	3.1 m
Primary Axis Diameter	2.4 m	1.5 m
Open/Closed Top	Open	Closed
Chugging Experienced	Yes	Yes
Inlet Steam Mass Flow Rate	0.3 kg/s	0.045 kg/s

From Table 1, it is shown that while both facilities have different orientations, they are similar in scale. While the POOLEX experimental facility employs a much larger Sparger, the steam flow rates are scaled such that the operating Reynolds number is approximately 100,000.

3.2 CFD Modelling of Direct Contact Condensation

CFD modelling of direct contact condensation presents many challenges. These technical challenges can be divided into the following categories:

1. Choosing a modelling framework that is suitable for simulating free surface flows with reasonable computational expense.
2. Finding adequate closure models for the Navier-Stokes equations.
    a. Correlations for heat transfer coefficients
    b. Drag models
3. Capturing flow characteristics of direct contact condensation flow regimes.
    a. Particularly difficult in the chugging regime

CFD modelling of direct contact condensation is still in its early stages of development. Most relevant literature in the computational realm of direct contact condensation modelling has been

published after the turn of the millennium. In this section, the breakthroughs that have been made with regards to these technical challenges are discussed.

3.2.1 CFD Modelling Framework for DCC Simulations

One of the principal challenges in CFD modelling of DCC involves spatially resolving thermal-hydraulic behavior at an interface between phases. It is often the case at this interface that there are substantial gradients in temperature, velocity, fluid properties, and phase volume fraction. With the presence of these large gradients over small volumes within a computational domain, resolving mass transfer at an interface can prove quite difficult with conventional interface tracking methods. Two methods used in free surface flows, the Volume of Fluid (VOF) and Eulerian two-fluid models, are described in this section as they relate to DCC modelling.

The most well-known interface tracking method, the VOF method, has been employed throughout literature in many multiphase flow problems. In this method, the following measures are taken when solving the Navier-Stokes equations:

1. The continuity equation is solved for the secondary phase in the system to find the volume fraction of the secondary phase. Typically, in nuclear system related applications, the primary phase is selected to be liquid unless the overall domain is predominantly of the vapor phase. In all volumes within the domain, the volume fraction of each phase must sum to unity, making it sufficient to solve the continuity equation for one phase [14].
2. A single momentum equation is solved. The momentum equation utilizes volume averaged properties (utilizing phase volume fraction), thus allowing the momentum equation to be solved for an effective mixture [14]. All phases possess the same velocity field.

3. The energy and turbulence transport equations are treated in the same way as momentum, with temperature and turbulence quantities shared by all phases.
4. By tracking the volume fraction in each cell of the computational domain, the location of the phase interface is effectively tracked. Getting reasonable quality spatial resolution of the interface requires careful selection of discretization schemes and mesh density.

In 2000, Meier et al. conducted experiments with air injection into a water pool. Using the VOF method, the evolution of an air bubble formation and detachment within the water pool was successfully demonstrated using a 2D mesh with success later also achieved with a 3D mesh [15].

However, when steam injection was later considered in their VOF model, difficulties arose. The reasoning for this difficulty is now very much made clear within commercial CFD software user manuals. When choosing the VOF method, it is imperative that the mesh grid be refined such that mesh size is smaller than the thermal-hydraulic phenomena being analyzed [14]. In the case of steam injection into a subcooled water pool, mass transfer must be resolved at an interface, and the length scale of this interaction can be influenced by turbulence characteristics at the interface. Therefore, if the turbulence length scales are small, the amount of grid refinement needed near the phase interface becomes prohibitive from the perspective of computational expense. Meier et al. also came to this conclusion stating:

"The direct numerical simulation of the full problem, including mass transfer, appears not feasible at present due to both methodical difficulties and limitations in computer power." [15]

In 2014, Li et al. performed a VOF simulation for steam injection into a water pool. Li et al. set the initial and boundary conditions within their model to be consistent with experimental tests performed by Chan and Lee in order to perform model validation. Within their model, the one

immediately obvious limitation is their high mesh density and the associated small time step of 1E-6 seconds [16]. Despite this limitation, their model was found to be capable of performing simulations of DCC and provided agreement with experimental test data from Chan and Lee.

The Eulerian Two-Fluid method is similar to the Volume of Fluid method in that liquid and vapor phases are allowed to interpenetrate within a volume of the computational domain. The Eulerian Two-Fluid model differs from the VOF method is that continuity, momentum, and energy equations are solved for each individual phase in the domain for a total of 6 equations in a case with two phases [14]. Turbulence is also treated the same way, with turbulence transport equations solved for each phase individually, ultimately leading to 4 more equations in a two-phase case assuming that a standard two equation turbulence model is used [14]. When compared with the VOF method, immediately it becomes apparent that this multi-phase modelling formulation introduces much more complexity due to the increased number of conservation equations along with the number of relations required for closure.

Where the Eulerian Two-Fluid model outperforms the VOF method is in its ability to capture two-phase interactions at an interface without requiring a prohibitively high mesh density and the consequent small time step requirements. According to Pellegrini et al., the reduced computational cost of using the Eulerian Two-Fluid model makes it a more ideal method for simulation of nuclear power plant systems on more realistic time scales of interest in plant design and safety analysis [17]. Therefore, the Eulerian Two-Fluid method has become the most promising development in DCC modelling over the past decade.

In 2014, Tanskanen et al. demonstrated the utility of the Eulerian Two-Fluid method through simulations of the POOLEX STB-28 experiments with the NEPTUNE_CFD software. Tanskenen et al. note that these experiments were performed within the chugging DCC flow regime [18]. In

their simulations, a 2D axisymmetric meshing approach was employed. Using a pattern recognition algorithm along with high speed cameras, Tanskanen et al. developed a method to experimentally assess the condensation rate of steam bubbles forming at the Sparger outlet [18]. Using the pattern recognition algorithm along with camera footage of bubble collapse, Tanskanen et al. attained simulation results that showed general agreement with experimental bubble size and chugging event frequency [18]. However, the condensation rates were not as well captured within their model, and they postulated that the weak initialization of turbulence in the model led to lower condensation rates than were exhibited in the true experimental conditions [18].

In 2015, Pellegrini et al. utilized the Eulerian Two-Fluid model within STAR-CCM+ to similarly simulate the STB 28-4 POOLEX experiment. However, Pellegrini et al. introduce a novelty to the model through the implementation of Rayleigh-Taylor instability theory to the interfacial area density closure relation [17]. Overall, their simulation found that the adjustment to the interfacial area density led to a large increase in interfacial surface area at the Sparger outlet, hence a higher condensation rate that induces violent chugging events [17]. Patel et al. performed simulations in 2017 of the same POOLEX test using both Open_FOAM and NEPTUNE_CFD with the implemented Rayleigh-Taylor instability correction, and the results achieved improved agreement with their experiment than compared to the results of Tanskanen et al. [13].

3.2.2 Rayleigh-Taylor Instability and Capturing DCC Flow Regimes

The Suppression Chamber CFD models created by Pellegini and Patel exhibit the importance of Rayleigh-Taylor Instability in modelling the chugging DCC flow regime. Rayleigh-Taylor Instability is a dynamic condition in multiphase flow where a smooth interface between two fluids becomes unstable due to pressure and density gradients near the interface in the presence of a local acceleration [19].

In a traditional case of Rayleigh-Taylor Instability, a light fluid is located below a heavier fluid and undergoes acceleration due to gravity. Intuitively, the denser fluid flows towards the lighter fluid in order to relieve the density gradient in the system. This causes the initial interface between the fluids to transition: an initially smooth interface takes on a wave-like pattern.

In the case of a Suppression Chamber, a steam bubble at the mouth of the Sparger is located above water. Dynamically, the steam bubble grows with inertia and condensation taking predominance in the rate of bubble growth. However, as the rate of bubble growth begins to stagnate, the impact of Rayleigh-Taylor Instability takes effect.

The instability begins at the steam-water interface in the presence of a pressure and density gradient, with the lighter fluid (steam) being located above the heaver fluid (water). Once the steam bubble growth stagnates, water is slowly accelerated towards the steam. This induces the Rayleigh-Taylor Instability at the interface with the wave-like pattern.

The instability at the steam-water interface generates an increase in interfacial surface area. As early as 1900, Lord Rayleigh studied this two-fluid dynamical behavior at an interface between incompressible and immiscible fluids. Through stability analysis, Lord Rayleigh proved that the wave amplitude (n) at the interface varies exponentially in time as shown in Equation 3.1 and Equation 3.2:

$$\sigma^2 = \frac{\rho_2 - \rho_1}{\rho_2 + \rho_1} \mathrm{k} = -\mathrm{A} * \mathrm{k} \tag{3.1}$$

$$\mathrm{n(t)} = \mathrm{n_0} e^{\sigma \mathrm{t}} \tag{3.2}$$

where ρ_2 is the density of the light fluid and ρ_1 is the density of the heavy fluid [19].

Equation 3.1 shows that the argument within the exponential, σ^2, is dependent on the Atwood number (A) which is commonly used in multiphase flow analysis to describe interfacial flow behavior. In Equation 3.1, the term, k, represents the wave number of the perturbed interface. In Lord Rayleigh's analysis, there is a critical wavenumber, k_c, which is ascribed to a transition from stable to unstable interfacial shape [19]. This critical wave number is formulated in the classical Rayleigh theory as follows:

$$k_c^2 = \frac{g(\rho_2 - \rho_1)}{T} \tag{3.3}$$

where g is the local acceleration and T is the surface tension.

Therefore, utilizing Equation 3.1 and Equation 3.3, the magnitude of the perturbation at the interface is described by Equation 3.2. The exponential dependence of interfacial area is one of the most important findings in this classical analysis. Initially, the perturbation at the interface is small which will only lead to modest increases in interfacial area. However, in a short time this perturbation becomes large, and the interfacial area increases quickly.

In context to bubble dynamics in a steam water system, the large increase in interfacial surface area due to Rayleigh-Taylor Instability leads to an increase in the condensation rate. In systems that are operating with steam mass flux and water subcooling within the chugging flow regime, the increased condensation rate due to Rayleigh-Taylor Instability leads to the condensation rate greatly exceeding the rate of steam mass flow into the Chamber, the condition necessary to cause a chugging event to occur. With Rayleigh-Taylor Instability models implemented by Pellegrini et al. and Patel, better quantitative agreement in the condensation rate was achieved with qualitatively larger chugging events as represented by water ascending well into the Suppression Chamber Sparger [17] [20].

In the analyses by Pellegrini et al. and Patel, Rayleigh-Taylor instability is considered with greater detail than the classical theory developed by Rayleigh. In 2013, Josey and Baglietto developed a more comprehensive treatment of interfacial area growth due to Rayleigh-Taylor Instability that accounted for a more significant effect of surface tension [21]. First, Josey and Baglietto assessed the formulations of Livescu which expands upon the classical treatment by Rayleigh as shown in Eq. 3.4 [22]:

$$\sigma^2 = \left(Ag - \frac{\sigma k^2}{\rho_1+\rho_2}\right)k \tag{3.4}$$

Utilizing the result by Livescu, the growth term in the exponential of Equation 3 was formulated by Josey and Baglietto leading to a final form shown in Equation 3.5 [21]:

$$\sigma = \text{Real}\left(\sqrt{\left(Ag - \frac{\sigma k^2}{\rho_1 + \rho_2}\right)k + \nu^2 k^4} - \nu k^2\right) \tag{3.5}$$

Equation 3.5 contains added terms which include the kinematic viscosity. Thus, the formulation of Josey and Baglietto accounts for compressibility, fluid viscosity, and enhanced treatment of the surface tension [21].

4. OBJECTIVES

The objectives of the proposed research are listed below. These objectives are listed in chronological order of necessary completion.

1. Develop a CFD model using STAR-CCM+ of the NHTS RCIC Pressure Suppression Pool facility
    a. The model must capture the relevant physics associated with direct contact condensation.
    b. The model boundary and initial conditions must be consistent with experimental conditions for a selected experimental test case at the NHTS facility.
    c. The model must be capable of demonstrating the presence of direct contact condensation flow regimes and provide insights into Pool mixing and future experimental design changes.
2. Improvements for future experimental design must be brought forward to enhance the capability to validate the model further.
3. Best practice guidelines for modelling direct contact condensation within the STAR-CCM+ Eulerian multiphase segregated flow model must be provided based on successes and failures in the current modelling effort.

5. PHYSICS MODEL SELECTION

In this section, the physics models implemented within STAR-CCM+ are described in detail. The models are separated into three categories: flow modelling, turbulence models, and closure relations.

5.1 Flow Modelling: Eulerian Multiphase Segregated Flow

STAR-CCM+ has a well-developed selection of multiphase flow models available. As described in Section 3.2.1, the Eulerian multiphase segregated flow model has been selected for this modelling effort due to its more relaxed requirements on mesh density near a phase interface which allows for longer time step sizes to be employed.

The Eulerian multiphase segregated flow model treats each phase present in the system independently leading to a set of conservation equations for each phase while maintaining a common pressure field for all phases in the system. For each conservation equation the sum of the volume fraction of each phase in each control volume must satisfy the relation:

$$\sum_{k} \alpha_k = 1 \tag{5.1}$$

The subscript k represents an individual phase within the system. In the remainder of this section the following convention is employed:

k = i (continuous phase, liquid water)

k = j (dispersed phase, steam)

In the Eulerian multiphase framework, the heaviest phase is commonly denoted as the continuous phase which in this analysis will be considered liquid water.

The following subsections provide the mass, momentum, and energy conservation equations used within the Eulerian multiphase segregated flow model. The equations are written with reference to the continuous phase (i), and a similar set of equations could easily be written for the dispersed phase (j) given the equations for the continuous phase.

5.1.1 Continuity Equation

Mass conservation in the Eulerian multiphase segregated flow model must account for mass transfer between the phases. This requires an extra term in the continuity equation when compared to a single-phase flow case. Equation 5.2 shows the integral form of the continuity equation employed for a given phase (i).

$$\frac{\partial}{\partial t}\int_V \alpha_i \rho_i dV + \oint_A \alpha_i \rho_i \mathbf{v}_i \cdot d\mathbf{A} = \int_V \sum_{j \neq i} (m_{ij} - m_{ji})\, dV + \cancel{\int_V \bar{S}_i^{\alpha} dV} \tag{5.2}$$

The first term on the right-hand side represents the mass transfer rate between phases i and j within the control volume. The final term on the right-hand side is a mass source term which is not needed for this case.

5.1.2 Momentum Conservation

Momentum conservation in the Eulerian multiphase segregated flow model contains similar terms to a single-phase formulation, but it must account for interphase momentum transfer along with mass transfer. The integral form of the momentum equation employed for phase (i) is shown below.

$$\frac{\partial}{\partial t}\int_V \alpha_i \rho_i \mathbf{v}_i dV + \oint_A \alpha_i \rho_i \mathbf{v}_i \otimes \mathbf{v}_i \cdot d\mathbf{A} = -\int_V \alpha_i \nabla p \, dV + \int_V \alpha_i \rho_i \mathbf{g} \, dV + \oint_A [\alpha_i (\mathbf{T}_i + \mathbf{T}_i^t)] \cdot d\mathbf{A} +$$

$$\int_V \mathbf{M}_i \, dV + \int_V \cancel{(\mathbf{F}_{int})_i dV} + \int_V \cancel{S_i^{\alpha} dV} + \int_V \sum_i (m_{ij}\mathbf{v}_j - m_{ji}\mathbf{v}_i) \, dV$$

The term $\mathbf{M}_i$ represents the interphase momentum transfer per unit volume which satisfies the following relation:

$$\sum_i \mathbf{M}_i = 0 \tag{5.3}$$

This relation meets the requirement that all interphase forces must balance. The interphase momentum transfer term contains all interaction forces between phases that the user selects to consider in the analysis as shown in Eq. 5.4:

$$\mathbf{M}_i = \sum_{j \neq i} \left(\mathbf{F}_{ij}^D + \cancel{\mathbf{F}_{ij}^{VM}} + \cancel{\mathbf{F}_{ij}^L} + \cancel{\mathbf{F}_{ij}^{TD}} + \cancel{\mathbf{F}_{ij}^{WL}} \right) \tag{5.4}$$

For this analysis, only the first term in the summation is considered: the interphase drag force ($\mathbf{F}_{ij}^D$). This drag force term requires a closure relation which is discussed in a following section. The virtual mass, lift, turbulent dispersion, and wall lubrication forces are not considered in the present analysis.

In Equation 5.4, the two terms struck out on the right-hand side represent the internal forces and momentum source term respectively. These are also not considered necessary for this analysis.

5.1.3 Energy Conservation

Energy conservation in the Eulerian multiphase segregated flow model must account for heat and mass transfer occurring between phases within the system. This leads to a core concept within the Eulerian multiphase segregated flow model: the phase interface.

5.1.3.1 Phase Interface Description

In each control volume, the Eulerian multiphase segregated flow model allows for both phases to be present with a corresponding volume fraction for each phase. In order to characterize the mass transfer interaction between phases within a control volume, the phase interface concept is employed. The phase interface is characterized by a saturation temperature, T_{ij}, which corresponds to system pressure. This interface serves as an intermediary to facilitate heat transfer between phases present in the system which is ultimately used to compute the mass transfer that occurs between the phases.

In the phase interface formulation, heat is transferred from a saturated phase interface to each phase in the system. Equations 5.5 and 5.6 show the heat transferred from the phase interface to phases i and j respectively. Note that a superscripted or subscripted (ij) denotes quantities at the phase interface.

$$Q_i^{ij} = h_i^{ij} a_{ij} \left(T_{ij} - T_i\right) \tag{5.5}$$

$$Q_j^{ij} = h_j^{ij} a_{ij} \left(T_{ij} - T_j\right) \tag{5.6}$$

Equations 5.5 and 5.6 contain the term a_{ij} which corresponds to the interaction area density. This describes the effective interfacial area present for heat and mass transfer at the phase

interface. A closure relation is required to compute the interaction area density in each control volume, and this is discussed in Section 5.3.

The terms h_i^{ij} and h_j^{ij} in Equations 5.5 and 5.6 correspond to the heat transfer coefficients for the continuous and dispersed phases respectively. These heat transfer coefficients are used to calculate the heat transfer from the phase interface to phases i and j and are computed as follows:

$$h_i^{ij} = \frac{Nu_i k_i}{l_{ij}} \tag{5.7}$$

$$h_j^{ij} = \frac{Nu_j k_j}{l_{ij}} \tag{5.8}$$

In Equations 5.7 and 5.8, the term l_{ij} corresponds to the interaction length scale at the phase interface. This term, like the interaction area density, also requires a closure relation discussed in Section 5.3. The Nusselt number for the continuous and dispersed phases, Nu_i and Nu_j, is computed through closure relations. In this analysis, only the Nusselt number for the continuous phase (i) is significant since steam temperature is always near the saturated phase interface temperature leading to negligible heat transfer from the phase interface to steam ($Q_j^{ij} \approx 0$).

5.1.3.2 Conservation Equation

The integral form of the energy conservation equation for phase (i) is shown below.

$$\begin{aligned}\frac{\partial}{\partial t}\int_V \alpha_i \rho_i E_i \, dV + \oint_A \alpha_i \rho_i H_i \mathbf{v}_i \cdot d\mathbf{A} + \oint_A \alpha_i p \, d\mathbf{A} \\ = \oint_A \alpha_i k_{eff,i} \nabla T_i \, d\mathbf{A} + \oint_A \mathbf{T}_i \cdot \mathbf{v}_i \, d\mathbf{A} + \int_V \mathbf{f}_i \cdot \mathbf{v}_i \, dV \\ + \int_V \sum_{ij} Q_i^{ij} \, dV + \int_V \cancel{S_{u,i} dV} + \int_V \sum_{j \neq i} (m_{ij} - m_{ji}) h_i (T_{ij}) dV\end{aligned}$$

In this formulation, heat conduction is considered using an effective thermal conductivity for phase i ($k_{eff,i}$), which is calculated as follows:

$$k_{eff,i} = k_i + \frac{\mu_{t,i} C_{p,i}}{\sigma_{t,i}} \tag{5.9}$$

where $\mu_{t,i}$ is the turbulent viscosity, $C_{p,i}$ is the specific heat capacity, and $\sigma_{t,i}$ is the turbulent thermal diffusion Prandtl number. This formulation for thermal conductivity provides a correction due to turbulence.

Mass transfer is considered in the sixth and seventh terms on the right-hand side of the energy equation. The sixth term, Q_i^{ij}, represents the heat transfer per unit volume from the phase interface to phase i. This term is computed using the same formulations shown in Equations 5.5 and 5.6. Heat transferred at the phase interface must balance with the seventh term, $(m_{ij} - m_{ji})h_i(T_{ij})$, which in this analysis represents heat given off by the steam per unit volume due to phase change (noting that for cases with only condensation $m_{ji} = 0$). This balance is shown in Equation 5.10.

$$Q_i^{ij} + Q_j^{ij} + (m_{ij} - m_{ji})\Delta h_{ij}(T_{ij}) = 0 \tag{5.10}$$

In this heat balance, the enthalpy of vaporization, $\Delta h_{ij}(T_{ij})$, is computed based on the temperature of the phase interface.

5.1.4 Steam and Water Properties

In order to compute certain thermodynamic field variables present in the conservation equations, the continuous and dispersed phases must be assumed to be either compressible or incompressible. In this analysis, steam and water thermodynamic properties are both computed

using IAPWS-IF97 property tables that are provided within STAR-CCM+. For further information about these property tables, refer to [23].

Steam must be considered compressible since drastic pressure changes can exist during direct contact condensation, particularly when a steam bubble collapses at the RCIC Sparger exit. For liquid water, the IAPWS property tables were used out of convenience, but this phase could also be considered incompressible with constant density for simplicity. The incompressible assumption can be considered valid as long as the temperature of the water does not change significantly during the simulated transient.

5.2 Turbulence Models

In this analysis, the standard k-ε turbulence model was selected for both the continuous and dispersed phases. This two-equation model yields a total of four more transport equations that must be solved along with the mass, momentum, and energy conservation equations for each phase.

In the Eulerian multiphase model, the general form of the turbulence transport equation is written as shown below.

$$\frac{\partial}{\partial t}\int_V \alpha_i \rho_i \phi_i \, dV + \oint_A \alpha_i \rho_i \phi_i \bar{\mathbf{v}}_i \cdot d\mathbf{A} = \oint_A \alpha_i \left(\mu_i + \frac{\mu_{t,i}}{\sigma_\phi}\right) \nabla \phi_i \cdot d\mathbf{A} + \int_V \alpha_i P_{\phi,i} \, dV -$$

$$\int_V \alpha_i D_{\phi,i} \, dV + \int_V \sum_{i \neq j} \left(m_{ij}\phi_j - m_{ji}\phi_i\right) dV$$

ϕ_i denotes the turbulence transport variable k or ε for phase i. The production terms, $P_{\phi,i}$ and $D_{\phi,i}$ depend on the turbulence model selection, which is in this case the k-ε model. Refer to [23] for more information on the specific production and loss terms for the k-ε model.

5.3 Closure Relations

From sections 5.1 and 5.2, it is shown that various closure relations are needed to completely solve the large set of conservation equations. The closure relations of most significant importance to the current work are discussed in detail in this section.

5.3.1 Drag Coefficient

In Equation 5.4, the drag force must be calculated to compute the interfacial momentum transfer term in Equation 5.3. This requires the use of a drag correlation which is used to compute a linearized drag coefficient which ultimately leads to a computed value for the drag force.

The symmetric drag law was selected for this analysis. According to the STAR-CCM+ user manual, the symmetric drag law is appropriate for situations where the dispersed phase in one region of the domain becomes continuous. This was deemed appropriate for this case since as a bubble forms on the outside of the Sparger, steam volume fraction within the bubble increases to near unity.

Equation 5.11 shows the linearized drag coefficient for the symmetric drag law:

$$A_{cd}^{D} = \frac{3}{4} C_D \frac{\alpha_i \alpha_j \left(\alpha_i \rho_i + \alpha_j \rho_j\right)}{\alpha_i l_i + \alpha_j l_j} |\mathbf{v}_r| \tag{5.11}$$

where $|\mathbf{v}_r|$ is the magnitude of the relative velocity between the continuous and dispersed phases and C_D is the standard drag coefficient. l_i is taken to be the interaction length scale which is later defined in Equation 5.15. l_j is the inverted topology length scale which was left at a default value of 1 mm.

5.3.2 Hughes-Duffey Nusselt number Correlation for DCC

In Equations 5.7 and 5.8, the Nusselt number is needed to compute heat transfer coefficients for water and steam respectively. Since steam is considered to be at saturated conditions with minimal heat transfer from the steam to phase interface, Nu_j, in Equation 5.8 was kept at the default value of 2 for all simulations. To compute the heat transfer coefficient on the liquid water side of the phase interface, Nu_i was computed using the correlation of Hughes and Duffey (1991). Equation 5.12 shows this correlation:

$$Nu_i = \frac{2}{\sqrt{\pi}} Re_{t,i}^{\frac{1}{2}} Pr^{\frac{1}{2}} \tag{5.12}$$

where Re_t is the turbulent Reynold's number and Pr is the Prandtl number for liquid water. The turbulent Reynold's number is computed based on liquid side turbulence parameters as shown below:

$$Re_t = \frac{u_{t,i} l_t}{\upsilon_i} \tag{5.13}$$

where l_t and $u_{t,i}$ are the turbulent length and turbulent velocity scales computed from the k-ε model.

$$u_{t,i} = C_\mu^{\frac{1}{4}} k_i^{\frac{1}{2}} \tag{5.14}$$

$$l_t = C_\mu \frac{k_i^{\frac{3}{2}}}{\varepsilon_i} \tag{5.15}$$

STAR-CCM+ does not currently have the Hughes-Duffey correlation available for use in the Continuous-Dispersed phase interaction model utilized in this study. Therefore, Equations 5.12-5.15 were implemented within STAR-CCM+ with user defined field functions.

5.3.3 Interaction Area Density and Length Scale

The interaction area density and interaction length scale play an important role in computing mass transfer terms as well as interphase drag force. It is important to select these values carefully to ensure that un-physical mass transfer rates are not obtained during the analysis.

The interaction area density was computed by taking the magnitude of the volume fraction gradient of the steam phase:

$$a_{ij} = |\nabla \alpha_i| \tag{5.16}$$

This method of computing the interaction area density is similar to the approaches used in Volume of Fluid methods.

The interaction length scale was selected to be the turbulent length scale of the liquid water, as shown in Equation 5.17. This combination of area density and length scale formulations led to the most successful results for this study in terms of physical significance. Overall, both of these closure terms required the use of user defined field functions for implementation.

6. NHTS FACILITY TEST CASE #4

In the NHTS Suppression Pool experiments, there were many Test Cases to choose from that have significant variations in operating conditions. For this work, Test Case #4 was selected to serve as the source of all conditions enforced in the CFD simulations.

This section outlines the operating conditions present in Test Case #4 which will be referenced throughout the following sections of the thesis. Furthermore, justification for using this test case is provided.

6.1 Test Case #4 General Description

Test Case #4 is considered a "mid-power standard alignment" case as stated by Solom [7]. Table 2 shows the operating conditions consistent with the mid-power standard alignment.

Table 2. NHTS Test Case #4 Operating Conditions and Parameters

Operating Parameters/Conditions	Parameter Description
Steam Generator Power	107 kW
Sparger Inlet Steam Temperature	120 ℃
Sparger Inlet Steam Quality	Approximately Saturated State
Steam Mass Flux	34 kg m^{-2} s^{-1}
Suppression Chamber Pressurization	No Venting
Average Vapor Space Pressure	180 kPa (at t = 4000 s)
Average Pool Water Temperature	67 C (at t = 4000 s)
Initial Pool Water Temperature	40 ℃

From Table 2, it is shown that this particular Test Case was run with no venting of the Suppression Chamber vapor space. Table 2 also provides a definition of the mid-power alignment which consist of steam entering the pool in an approximately saturated state at 120 ℃.

At this saturation temperature, the corresponding steam mass flux was held fixed at 34 kg m^{-2} s^{-1}. The significance of using this mass flux of steam can be extracted from the following flow regime map in Figure 4.

As shown in Figure 4, Test Case #4 falls within the chugging region of the DCC regime map based on the subcooling and Sparger inlet steam mass flux. Over the course of the test case, the Suppression Pool water temperature increases, reaching the bubbling regime.

6.2 Justification for Using Test Case #4

Test Case #4 for simulations in this work due to the fact that it exhibited behavior consistent with multiple DCC flow regimes. As stated by Solom, this test case showed "clear chugging and temperature stratification profiles" making it a "quintessential RCIC test case" [7].

Evidence for this behavior is shown in Figure 8 as developed by Solom in [7]. For approximately 3000 seconds of this Test Case, Pool axial temperatures showed no stratification which is a characteristic of well mixed conditions induced by the chugging DCC flow regime. However, at approximately 4000 seconds into the test, axial temperature stratification is initiating between the lower and upper regions of the Suppression Pool which is indicative of the onset of the bubbling DCC flow regime.

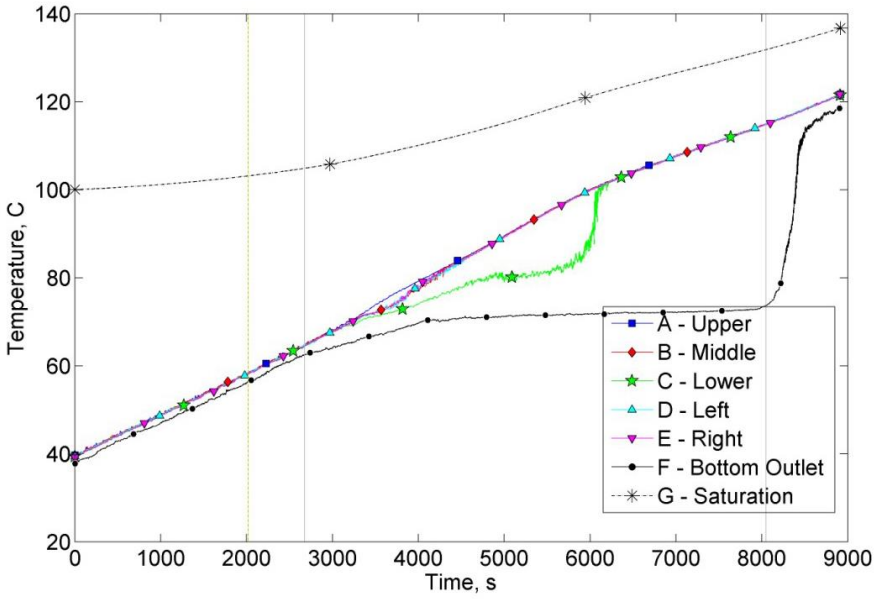

Figure 8. Suppression Pool Temperature Progression Test Case #4 [7]

With the varying degrees of subcooling present in this Test Case (and consequent variation in DCC flow regimes), Test Case #4 provided a well diverse set of possible conditions to consider for CFD simulations. Among the other test cases, one of the main differences is venting of the Suppression Chamber vapor space to atmosphere. Other differences include steam operating temperature and mass flux entering the Suppression Chamber Sparger.

7. NHTS TEST CASE #4 MODEL DEVELOPMENT

In this section, the model development in STAR-CCM+ for the NHTS Facility Test Case #4 is presented.

7.1 NHTS Facility Geometry

The NHTS Facility (depicted in Figure 5 and Figure 6) is a horizontally oriented pressure vessel with a roughly cylindrical shape when excluding the two end caps. The initial water level within the Suppression Chamber is approximately 0.78 m.

For this work, the primary goal was to examine steam-water condensation behavior near the exit of the Suppression Chamber Sparger. This goal varies significantly from the goals of the original NHTS Facility experimental tests which were considering bulk pool temperature stratification.

Given that the bulk pool behavior far from the Sparger was not of interest in this work, it was decided to consider a simplified geometric domain. This simplification preserved important characteristics of the NHTS Suppression Chamber geometry while also allowing for the utilization of symmetry. Figure 9 shows a CAD representation of the simplified NHTS Suppression Chamber domain.

In Figure 9, ¼ of the domain is shown. The blue region is the NHTS Sparger while the green region represents the Pool water domain within the Suppression Chamber. With the Suppression Chamber Sparger located in the center of the overall cylindrical Suppression Pool region, cylindrical symmetry was able to be utilized which is discussed with more depth later in this section.

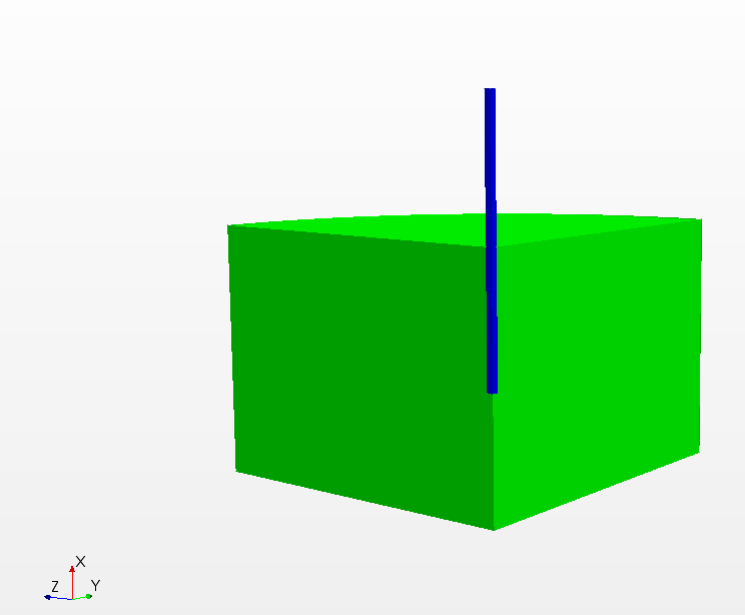

Figure 9. Simplified Suppression Chamber CAD Representation

Overall, Table 3 shows the important geometric characteristics of the NHTS Suppression Pool domain.

Table 3.NHTS Test Case #4 Operating Conditions and Parameters

Suppression Pool Geometric Parameters	**Parameter Values**
Suppression Pool Water Height	0.78 m
Suppression Pool Water Volume	2.75 m^3
Suppression Chamber Sparger Outlet Height	0.381 m
Suppression Chamber Sparger Length	0.819 m
Suppression Chamber Sparger Diameter	4.1 cm

From Table 3, the Suppression Pool water volume and height are preserved with respect to the actual NHTS Suppression Pool Geometry. With respect to the Sparger, the diameter is preserved such that the prescribed steam mass flux in Test Case #4 corresponds to the correct mass flow rate.

Ultimately, utilizing this simplified domain gives rise to the possibility of utilizing axisymmetry in all simulations performed. Within STAR-CCM+, the axisymmetric approach considers a 1 radian slice of the geometric domain. This greatly reduces computational cost of all simulations since the number of mesh cells utilized in the simulations is reduced greatly. However, the drawback to utilizing the axisymmetric approach lies in the fact that bubble formation is not necessarily symmetric around the vertical axis. While a full 3D representation would be ideal to capture any asymmetries, the computational cost was deemed too great for the time of this work.

7.2 Meshing Strategy

Employing the 2D-axisymmetric approach in STAR-CCM+ requires the creation of a 3D volume mesh and subsequent conversion to 2D. Note, that in order to utilize the 2D-axisymmetric model, the entire domain must lie above $y = 0$ m with a plane existing at $z = 0$ m.

Both structured and unstructured meshing strategies were employed in this work. To create a structured mesh, the STAR-CCM+ directed meshing tool was implemented. This creates a volume mesh that consists of blocks which then project to quadrilaterals in 2D. The unstructured mesh was generated using the STAR-CCM+ automated meshing tool. This was used to create a volume mesh that consists of polygonal cells.

7.2.1 Polygonal Meshing Strategy

The unstructured volume mesh for the NHTS Suppression Pool domain was created utilizing polygonal mesh cells with corresponding prism layers along all wall boundaries. Furthermore, in order to adequately capture the steam-water interactions (primarily condensation), grid refinement was required near the Sparger outlet where bubble formation takes place. This was accomplished using a volumetric control within a 6 cm radius sphere centered on the Sparger outlet. Finally, a cylindrical volumetric control was enforced inside the Sparger to maintain reasonable cell sizes inside the Sparger above the spherical refinement zone.

Overall, Figure 10 and Figure 11 show the final converted 2D mesh developed.

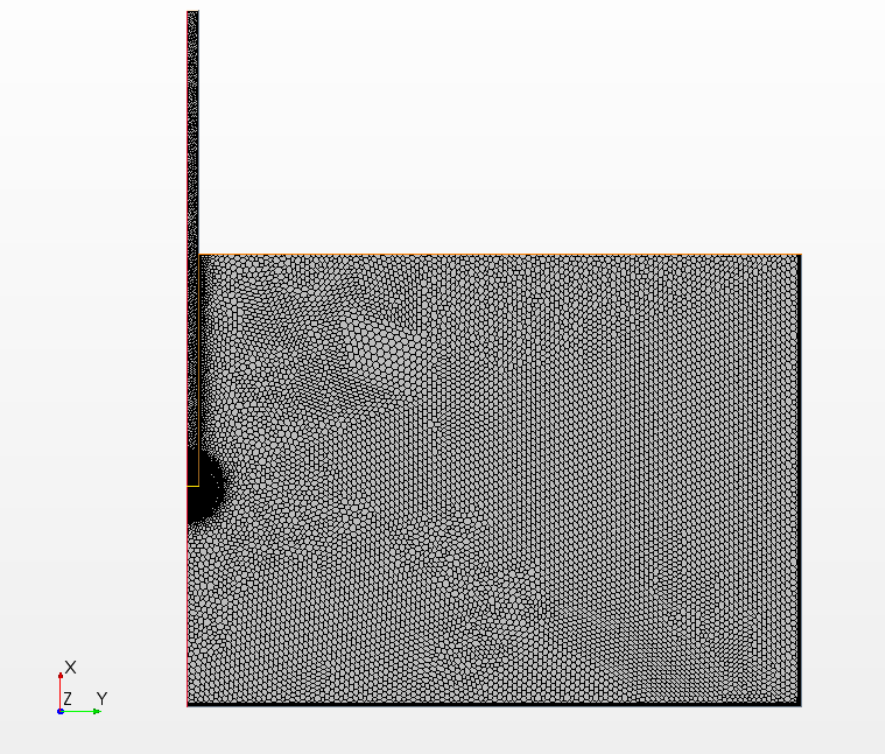

Figure 10. Converted 2D Mesh of NHTS Suppression Chamber

From Figure 10, the spherical refinement zone is shown clearly as well as refinement above this zone inside the Sparger. Figure 11 shows a zoomed in view of the spherical refinement zone.

In order to produce this mesh, some important automated mesh settings in STAR-CCM+ were utilized as shown in Table 4.

Table 4. Automated Mesh Parameters Used in STAR-CCM+

Automated Mesh Parameters	**Parameter Setting**
Base Cell Size	5 cm
Target Surface Size	1 cm
Number of Prism Layers	3
Prism Layer Near Wall Thickness	1 mm
Prism Layer Total Thickness	3 mm
Spherical Volumetric Control Cell Size	2 mm (nominal) , 4 mm (coarse)
Cylindrical Volumetric Control Cell Size	4 mm

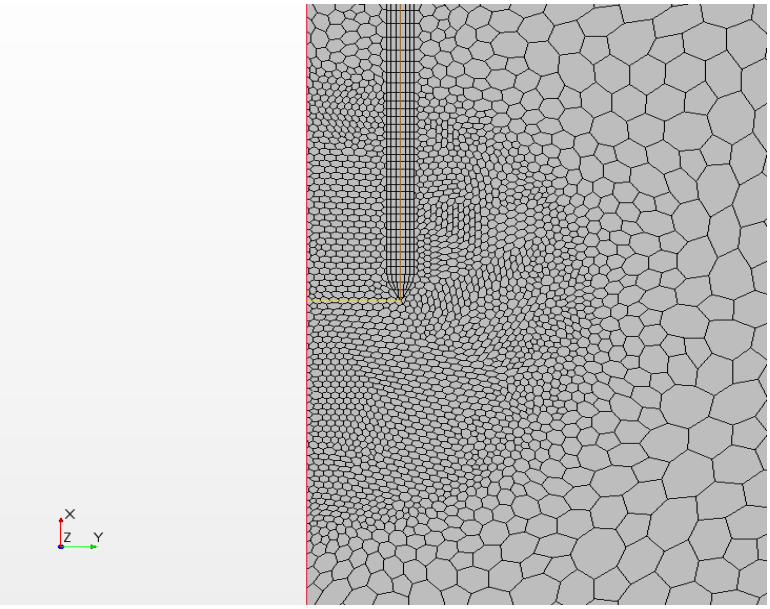

Figure 11. Spherical Refinement Zone in Polygonal Mesh (2 mm refinement)

From Table 4, the prism layer near wall thickness was selected in order to generate Wall Y+ values > 30 which is consistent with the use of a High Y+ turbulence model. Within the spherical volumetric control, it is shown that there were two refinements considered for analysis, a 4 mm coarse refinement and a 2 mm nominal refinement. In Section 9, the influence of the selection of grid refinement is discussed at length.

7.2.2 Directed Meshing Strategy

In STAR-CCM+, the directed meshing tool was used to create the structured grid. In order to do this, the tool takes source and target surfaces within the geometry as defined by the user. Upon selecting these surfaces, the user then is able to define a 2D grid on the source surface. The user can choose the spacing within the grid by implementing either constant grid spacing or spacing based on geometric or hyperbolic gradient.

With this 2D grid defined on the source face, the volume mesh is generated by sweeping between the defined source and target face. For the NHTS CAD geometry source faces were defined in the Sparger and Pool regions. These faces were chosen to lie on the z = 0 plane for each region. Corresponding target faces were taken on the y = 0 plane of the CAD geometry in Figure 9.

Given the definition of source and target faces, the 2D grids were generated for each the Sparger and Pool regions. The grid was defined using the geometric gradient grid spacing in both the x and y directions. For this work, three overall structured meshes were generated for use in a grid convergence study. Table 5 shows the cell sizes used in the refined region near the Sparger outlet.

Table 5. Structured Grid Parameters

Parameter	**Value in Directed Mesh**
x,y direction Cell Sizes	2 mm – 5 mm gradient – Grid C 2-3 mm constant – Grid D 1-2 mm gradient – Grid E
Near Wall Cell Thickness	1 mm

Overall, Table 5 shows that the refinement in the x and y direction was lowered for each subsequent generated grid. The y-direction gradient satisfied that near wall cell thickness would give wall y+ >30. Figure 12 shows an overall view of the refined Pool region of the directed

mesh after the volume mesh was converted to 2D. The yellow line indicates the outlet of the Sparger and the red line indicates the axis oriented in the +x direction.

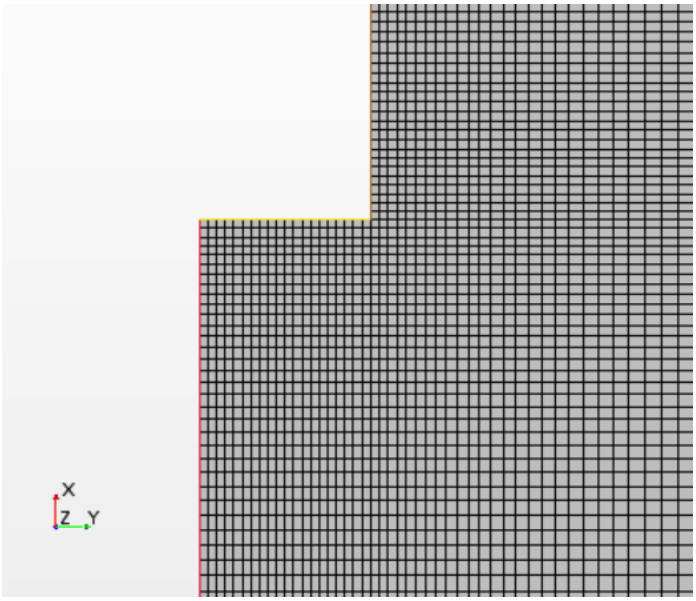

Figure 12. Directed Mesh of Pool Region Near Sparger (1-2 mm gradient)

7.3 Initial and Boundary Conditions

In Subsection 7.2, the overall geometry and mesh utilized is shown. Figure 13 shows the corresponding boundaries on the 2D plane. From Figure 13, it is shown that axis symmetry is employed along the x-axis in the z = 0 plane. Steam enters the domain through a mass flow inlet, and the water surface within the pool is maintained at a constant pressure through the use of a pressure outlet boundary. All walls in the domain are considered adiabatic to remove added complexity of conjugate heat transfer through both the Sparger and Suppression Chamber walls.

The mass flow inlet boundary condition was employed since steam mass flux was maintained constant during experiments at the NHTS facility. Utilizing a velocity inlet boundary condition,

as employed by Pellegrini et al. in [17], was found later to cause variations in steam inlet mass flux to the Sparger due to pressure transients that cause variation in steam density.

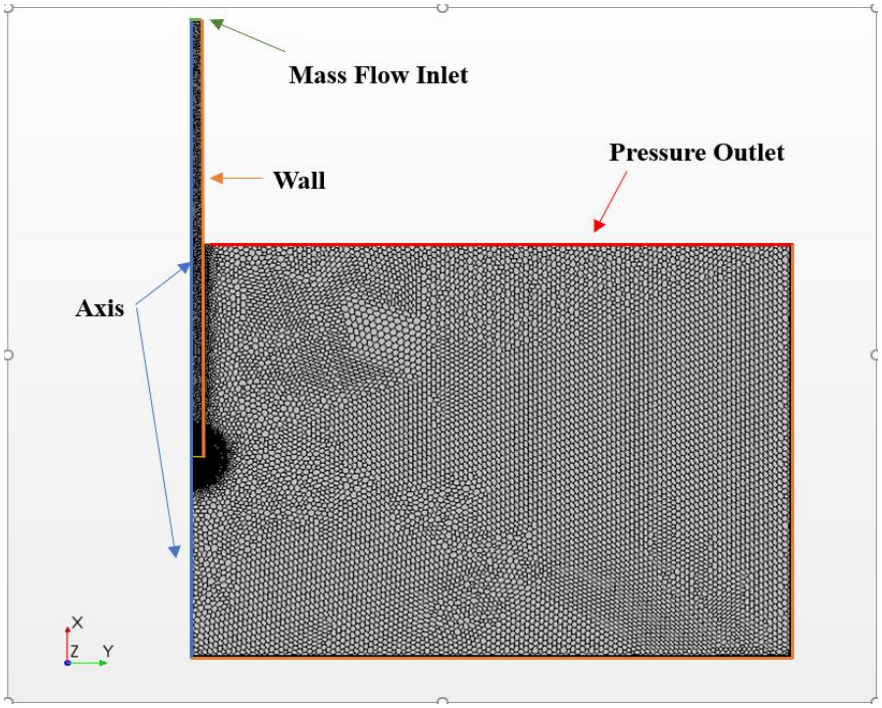

Figure 13. Boundaries on 2D Projected Domain

Within STAR-CCM+, when two regions of the domain share a common boundary, an interface condition is required. In this case, the Sparger region and Suppression Pool share a wall boundary. This wall was considered taken to be zero thickness which translates to a baffle interface. The outlet of the Sparger intersects the Suppression Pool domain and is treated as an internal interface allowing the transfer of steam from the Sparger to the Suppression Pool.

Given the definition of the boundaries in the domain, the next step is to define the steam and water conditions that exist at those boundaries as well as initial conditions of steam and water

inside the Sparger and Suppression Pool. In order to do this, the operating conditions of NHTS Test Case #4 were considered (from Table 2).

In Table 2, the steam inlet mass flux and temperature are defined as well as the average pressure conditions in the Suppression Chamber vapor space. These identical operating conditions are utilized in all subsequent analyses of this work. However, for the pool water temperature, the average temperature in the Suppression Pool corresponding to this vapor space pressure condition was utilized. All average values correspond to approximately t = 4000 sec in the Test Case #4 experiment.

Table 6 shows the parameters for the mass flow inlet boundary.

Table 6. Mass Flow Inlet Boundary Condition Parameters

Phase	**Water**	**Steam**
Mass Flux	0	34 kg m^{-2} s^{-1}
Volume Fraction	0	1
Temperature	T_{sat} [197 kPa]	T_{sat} [197 kPa]
Turbulent Intensity	-	0.0379
Turbulent Length Scale	-	0.0028 m
Turbulent Kinetic Energy	1E-4 [m^2s^{-2}]	-
Turbulent Dissipation Rate	1E-3 [m^2s^{-3}]	-

Table 7 shows the parameters for the pressure outlet boundary condition.

Table 7. Pressure Boundary Condition Parameters

Phase	**Water**	**Steam**
Volume Fraction	1	0
Temperature	67 °C	T_{sat}
Turbulent Kinetic Energy	1E-3 [m^2s^{-2}]	1E-3 [m^2s^{-2}]
Turbulent Dissipation Rate	1E-4 [m^2s^{-3}]	1E-4 [m^2s^{-3}]
Pressure	180 kPa	180 kPa

From Table 6 and Table 7, saturation temperature is computed from the IAPWS steam table in STAR-CCM+. For the pressure outlet boundary, little turbulence is expected at the boundary due to its far proximity from the Sparger outlet, therefore these values were intentionally set low. The initial conditions for steam and water in the domain are shown in Table 8.

Table 8. Initial Conditions Test Case #4

Phase	**Steam**	**Water**
Pressure	197723 Pa	Hydrostatic+Vapor Space P
Volume Fraction	1 (Inside Sparger)	1 (outside Sparger)
Temperature	Saturation Temperature	67 °C
k [m^2s^{-2}] and ε [m^2s^{-3}]	1E-4 and 1E-3	1E-4 and 1E-3
Velocity	0 m/s	0 m/s

Table 8 shows the initial conditions in the Sparger and Suppression Pool regions of the domain. The volume fraction of steam was set to 1 inside the Sparger with water completely filling the Suppression Pool region. This was done due to the absence of any knowledge of the true initial steam-water interface inside Suppression Chamber at the time in the experiment corresponding to a Suppression Chamber vapor space pressure of 180 kPa.

Steam pressure was set based on saturation condition at 120 ℃. Water pressure was set based on the hydrostatic pressure plus the initial 180 kPa inside the Suppression Chamber vapor space above the water level of the Suppression Pool.

The pool was considered to be at a static velocity due to lack of data to justify a more realistic condition. Consequently, turbulence parameters in the system were also set to a low value to reflect this "static start" condition.

Table 9 shows steam and water thermodynamic properties used for this analysis.

Table 9. Thermodynamic Properties Test Case #4

Phase	**Steam**	**Water**
Dynamic Viscosity	1.295E-5 Pa-s	4.22E-4 Pa-s
Heat of Formation (Enthalpy)	2705 kJ/kg	0.279951 kJ/kg
Standard State Temperature	120 ℃	67 ℃
Specific Heat	f(T,P)	f(T,P)
Thermal Conductivity	0.02745 W/m-K	0.661 W/m-K

In Section 5.1, the use of IAPWS steam and water thermodynamic properties was discussed. In Table 9, it is shown that dynamic viscosity and thermal conductivity were treated as constant rather than varying with temperature and pressure. This is a simplification to help with numerical stability. Heat of formation and standard state temperature are critical parameters that are needed to help calculate the latent heat of vaporization for the steam-water condensation interaction. Given the standard state temperature and enthalpy, STAR-CCM+ is able to calculate the enthalpy of each phase given temperature and pressure. In this analysis, the heat of formation and standard state temperature were set to the enthalpy of saturated steam and the temperature of 120 °C. Likewise, the heat of formation of water was set to the enthalpy of water at the temperature of 67 °C.

Finally, two parameters of importance to computing the condensation rate must be set: the phase interface temperature and latent heat of vaporization. The phase interface temperature, T_{ij}, in Equations 5.5 and 5.6 was set to the saturation temperature of steam at the given system pressure (computed from the IAPWS tables). The latent heat of vaporization, as noted in the previous paragraph, is also computed internally from IAPWS tables. This formulation for these two parameters allows the parameters to vary during pressure transients in the system.

7.4 Reference Parameters

In STAR-CCM+, reference parameters are chosen in in order to aid in numerical stability of simulations as well as to set global terms such as gravitational acceleration. The relevant reference parameter settings are shown in Table 10.

Table 10. Reference Parameter Selection

Reference Parameter	Parameter Setting
Pressure	180 kPa
Density	1.12 kg/m^3
Gravitational Acceleration	-9.81 m/s (x-direction)

The reference pressure was set to the Suppression Pool vapor space pressure of 180 kPa. This setting is necessary to set what STAR-CCM+ refers to as the piezometric (or operating pressure). The operating pressure is set by subtracting the reference pressure from the absolute pressure in the domain. It is this operating pressure that is utilized in the numerical model formulations described in Section 5. By using this reference pressure, the operating pressure is an order of magnitude less than the absolute pressure which aids in numerical stability.

The reference density was set to the density of the lightest phase (in this case steam). When calculating operating pressure, the hydrostatic contribution of steam will thus be minimal. Finally, gravitational acceleration was set in the x-direction consistent with the vertical axis in this domain existing the +x direction.

8. SIMULATION NUMERICAL SETTINGS

In this section, the numerical model settings utilized in STAR-CCM+ are discussed. Before proceeding, note that a double precision version of STAR-CCM+ was used. This is common for multiphase applications.

8.1 Time Discretization and Time-Step Size

In all simulations a first order backward Euler implicit time step discretization was utilized. The time-step size was determined based on a user imposed Courant number limit. For the current work, a maximum Courant number of 10 was observed throughout the simulations with the average maximum Courant number over the simulations being much less than this limiting value. It was found that exceeding a Courant number of 1 was acceptable in work by Pellegrini et al., and in this work it was likewise noted that a Courant number below 10 did not substantially impact observed flow and condensation behavior.

Unfortunately, STAR-CCM+ does not have a Courant number limited variable time-step setting in the Eulerian Multiphase Segregated Flow model. While this has been recommended to Siemens as a future addition to the code, the present analysis required the manual creation of a variable Courant number limited time-step. To do this, STAR-CCM+ reports were used to determine the maximum velocity and minimum cell size in the domain at each time-step. Then, the time-step size was set based on the following equation:

$$\Delta t = \frac{\Delta x_{min}}{u_{max}} CFL_{max}$$

While this is not a perfect method, the Courant number was limited in these simulations such that the Courant number was well below 10.

8.2 Other Discretization Schemes

The discretizations for other fields in this analysis are shown in Table 11.

Table 11. Discretizations for Fields

Field	Order of Discretization
Velocity Convection	2nd
Volume Fraction Convection	2nd
Temperature (Steam and Water)	2nd
Turbulence (Steam and Water)	2nd

These discretization schemes were set based on the defaults in STAR-CCM+. Higher order schemes are available, but they were found to lead to difficulties in convergence.

8.3 Relaxation Factors

In multiphase CFD simulations, setting appropriate relaxation factors is necessary to achieve desired convergence during each time-step. Table 12 shows the relaxation factors used for various solver fields in this analysis.

Table 12. Relaxation Factors for Solver Fields

Solver Fields	Overall Relaxation Factor
Phase Coupled Velocity	0.56
Pressure	0.2
Volume Fraction	0.1
Energy	0.3
Turbulence	0.3

8.4 Convergence Criterion

In all simulations, convergence was deemed to be reached for each time-step when RMS residuals less than 1E-4 for all fields. Furthermore, during each time step, the total mass transfer rate was monitored to ensure that the mass transfer rate reached a steady value before proceeding over the course of all inner iterations of a time step. The standard for convergence in mass transfer rate was set such that the mass transfer rate did not vary by more than 1% of inlet steam mass flow rate over 50 inner iterations of a time step similar to the convention used in [17].

At some times in the simulations, the energy residuals for water had difficulties in reaching RMS values less than 1E-4. In this case, convergence for a time-step was assessed based on the mass transfer rate using the above criterion.

9. SIMULATION RESULTS

In this section, the results of multiple simulations of the NHTS Test Case #4 are shown. First, a grid convergence study was performed to identify an adequate mesh size inside the refined regions of the Pool near the Sparger outlet. Using this identified mesh from the grid convergence study, a full simulation of bubble formation and deformation was performed. The results of this simulation are examined both qualitatively and quantitatively with respect to parameters of interest to direct contact condensation flow regimes.

9.1 NHTS Test Case #4 Grid Convergence

Assessing the sufficiency of the grid refinement near the NHTS Sparger outlet requires both qualitative and quantitative assessments with multiple grid sizes using both the structured and unstructured meshing strategies. For this grid convergence study, the following enforced cell sizes in the refined region of the unstructured mesh were used as shown in Table 13.

Table 13. Cell Sizes for Unstructured Mesh Grid Convergence Study

Simulation Grid	Refined Region Cell Size
A	4 mm
B	2 mm

In Table 14, the enforced cell sizes in the refined region of the structured meshes are shown.

Table 14. Cell Sizes for Structured Mesh Grid Convergence Study

Simulation Grid	Refined Region Cell Size
C	2-5 mm geometric gradient
D	2-3 mm
E	1-2 mm

Each simulation was run with initial and boundary conditions as shown in Table 6, Table 7, and Table 8. Steam and water properties were specified as listed in Table 9. In order to assess grid convergence, three quantities of interest were considered as listed below:

- Condensation Mass Flow Rate ($\dot{m}_{ij}$ from Equation 5.11)
- Bubble Interfacial Area
- Bubble Penetration Depth

The condensation mass flow rate was computed within STAR-CCM+ as the volume integral of the interphase mass transfer rate ($\dot{m}_{ij} - \dot{m}_{ji}$) in Equation 5.11) where $\dot{m}_{ji}$, representing boiling mass transfer of water to steam, is zero. Bubble interfacial area was likewise computed as a volume integral of the interaction area density (a_{ij}). Penetration depth was taken at the furthest extent of bubble formation in the -x direction.

It is important to note that when using the axisymmetric approach in STAR-CCM+, all quantities that have any volume dependence must be multiplied by 2π radians to get the correct value for the quantity over the full geometric domain. Also, all computed integrals and sums considered only the Pool region where the primary steam-water interface is located.

Each of these quantities of interest was selected due to their relationship and importance to flow dynamics and mass transfer. Mass transfer poses the most significant challenge in this modelling effort due to its effect on mass and energy conservation. Flow dynamics must also be

accurately captured since parameters such as bubble interfacial area directly affect the condensation mass flow rate in the system.

9.1.1 Polygonal Mesh Comparison

First, the two grids with the polygonal meshing strategy were compared with respect to the listed parameters of interest. Table 15 shows the resulting parameters at t = 8.6 ms of the transient.

Table 15. Grid Convergence Assessment of Polygonal Mesh Grids

Parameter	**Grid A**	**Grid B**	**Percent Difference** (Grid A to Grid B)
Condensation Mass Flow Rate	0.0173 kg/s	0.02 kg/s	-14.5%
Bubble Penetration Depth	3.4 cm	3.2 cm	+6.1%
Bubble Interfacial Area	293 cm^2	256 cm^2	+13.5%

From Table 15, the two parameters that exhibit the most significant difference are condensation mass flow rate and bubble interfacial area. Condensation rate is directly proportional to bubble interfacial area density through Equations 5.5 and 5.6 which compute the rate of heat transfer per unit volume between each phase and the phase interface. These equations feed into Equation 5.10 to compute the condensation rate per unit volume.

Intuitively, a greater bubble interfacial area should lead to a higher rate of condensation. However, Table 15 shows that opposite behavior was exhibited. Therefore, the difference in the condensation mass flow rate is likely due to differences in the value of the heat transfer coefficient, h_i^{ij} (from Equation 5.8). The heat transfer coefficient is directly proportional to the Nusselt number and inversely proportional to the turbulent length scale. The Nusselt number, computed using the Hughes-Duffey correlation, depends on the turbulent Reynold's number. Hence, the value of the heat transfer coefficient has a strong dependence on turbulence in the water.

With the importance of water turbulence recognized, an explanation for the difference in condensation mass flow rate was easily pinpointed by first taking an average of the product of the heat transfer coefficient and the interaction area density within a 3 cm radius circle centered on the Sparger outlet for each grid. Next, the average interaction area density was computed on each grid using the same circular area. The average interaction area density for Grid A was 8% greater than Grid B, but the product of the heat transfer coefficient and the interaction area density was 16.1% higher in Grid B. This proves that a difference in the heat transfer coefficient is the primary contributor to the discrepancy in condensation mass flow rate.

Ultimately, this result is indicative of inadequate capturing of turbulence in the water since the most critical quantities utilized to calculate the heat transfer coefficient are dependent on water turbulence parameters.

Given this result, the simulation utilizing Grid B was continued to assess flow behavior beyond 8.6 ms. As the simulation progressed, it was found that Grid B began to exhibit divergence in turbulence parameters that led to a failed simulation.

Therefore, the unstructured mesh was deemed to be unsatisfactory for further analysis. In future work, further consideration of this unstructured mesh strategy could be employed, but the following issues would need to be rectified:

- Poor cell quality near the axis boundary of the Sparger
- Poor cell quality in prism layer cells located near the Sparger outlet

9.1.2 Structured (Directed) Mesh Comparison

After completing the study of the unstructured meshes, the structured meshing strategy was similarly assessed. Simulations utilizing these structured meshes exhibited much better convergence of turbulence parameters as well as faster run times when compared to the unstructured grids. Therefore, a 30 ms transient was simulated with each mesh listed in Table 14, and all quantities of interest were compared.

First, the condensation rate achieved during each simulation with the three grids was considered. Figure 14 shows the condensation rate over the entire 30 ms transient for each grid. From Figure 14, it is apparent that the coarsest refinement (Grid C) gave the lowest maximum condensation rate with the maximum achieved condensation rate increasing as the grids became more refined. Table 16 shows the maximum condensation rate achieved using each mesh.

Table 16. Maximum Condensation Rate during 30 ms Transient using Structured Grids

Simulation Grid	Maximum Condensation Rate (g/s)	Time Achieved (ms)
C	37.1	20.4
D	45.3	19.3
E	48.8	19.5

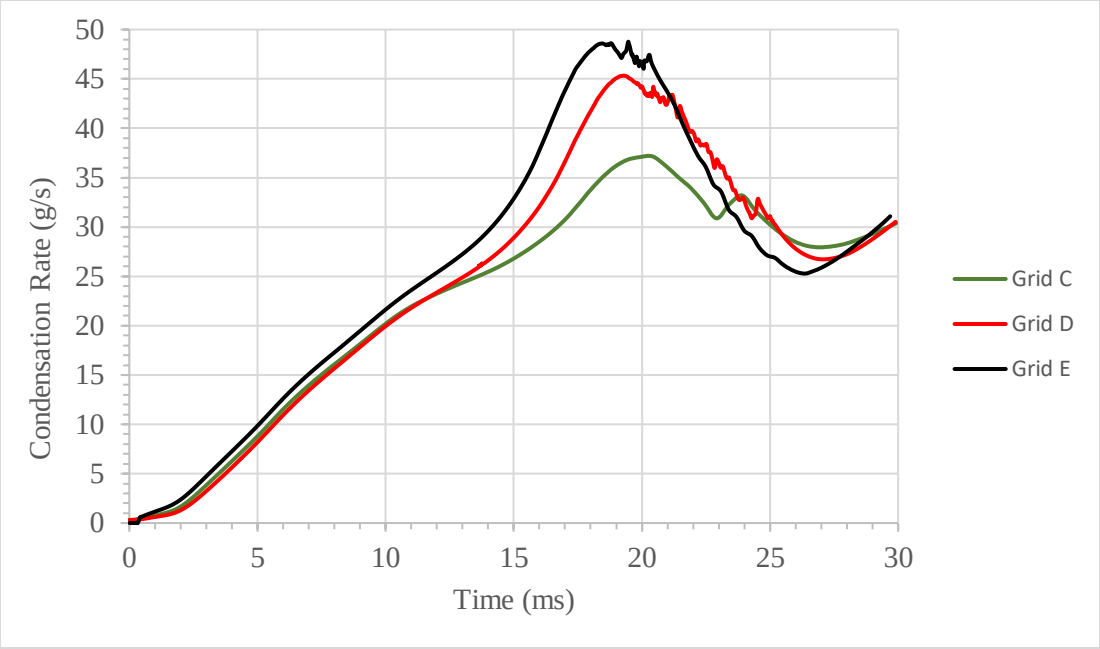

Figure 14. Condensation Rate during 30 ms Transient with Grids C, D, and E

The percent difference between the maximum condensation rates achieved in Grids C and D is 19.9 percent. The percent difference between the maximum condensation rates achieved in Grids D and E is 7.4 percent.

The times that the maximum condensation rate was achieved were similar for Grids D and E while Grid C lagged behind by approximately 1 ms. Thus, the start time of the bubble deformation process in each grid was found to be quite similar for each grid. During the bubble deformation process, the total interfacial area decreases as steam begins to condense in the Pool. Figure 15 shows the total bubble interfacial area over the 30 ms transient.

From Figure 15, it is shown that indeed the start of the bubble deformation process occurs at a similar time for each grid. However, the decrease in total interfacial area due to condensation is severely different between Grid C and the more refined grids. This is an expected result given

the much lower maximum condensation rate achieved using Grid C leads to less overall deformation of the steam bubble.

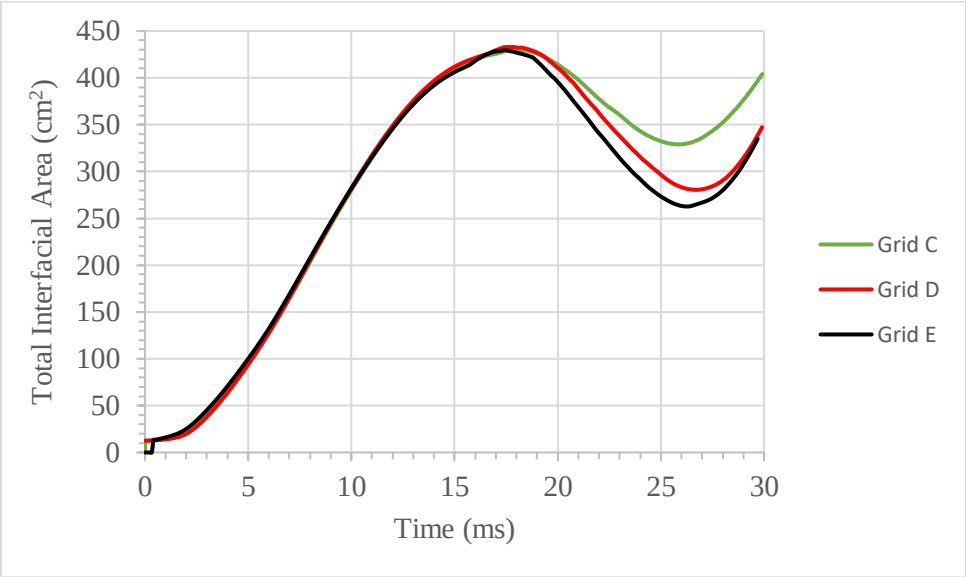

Figure 15. Total Interfacial Area during 30 ms Transient with Grids C, D, and E

The bubble deformation took place between t = 18 ms and t = 30 ms. The resulting final profile of the steam volume fraction at t = 30 ms for each grid is shown in Figure 16.

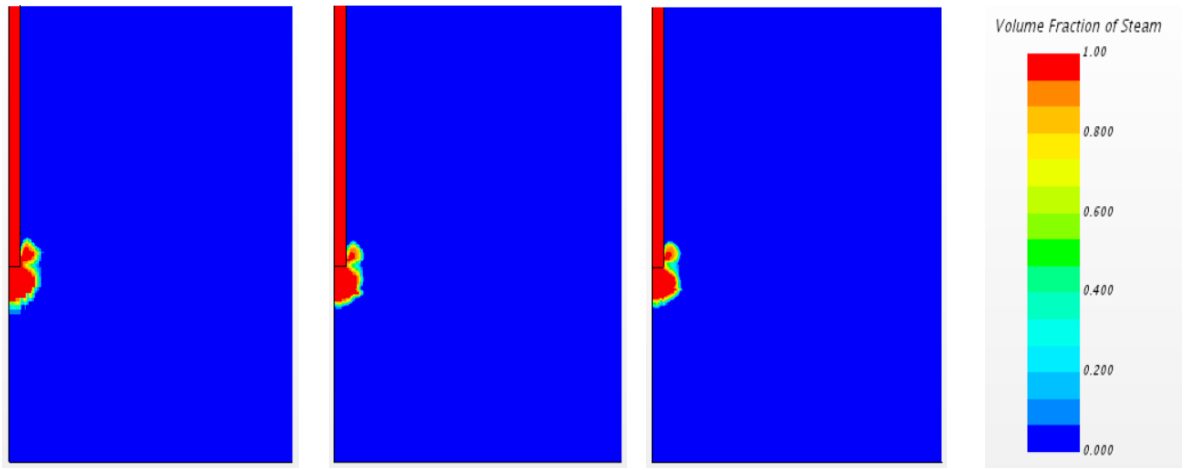

(a) (b) (c)

Figure 16. End of Bubble Deformation at t = 30 ms for (a) Grid C (b) Grid D (c) Grid E

From Figure 16, it is shown that the bubble does not fully collapse which is more characteristic of the bubbling direct contact condensation flow regime. In each grid, the bubble deforms creating two steam pockets, one above the outlet of the Sparger and one below the outlet of the Sparger. However, for Grid C, the steam pocket above the Sparger outlet does not exhibit as much separation from the core bubble below the Sparger as observed in Grids D and E. This is a byproduct of having a much lower condensation rate at the start of the deformation.

One interesting result exhibited in Figure 15 is that the maximum total interfacial area achieved in each grid was similar. Given this result, intuition may suggest that the condensation rates achieved in each grid should also be similar in magnitude. However, this was not found to be the case. To investigate this result, the steam volume fraction within the Pool region was assessed for each mesh. Figure 17 below shows the steam volume fraction for Grids C, D, and E at t = 18.6 ms, 18 ms, and 19 ms respectively for each grid.

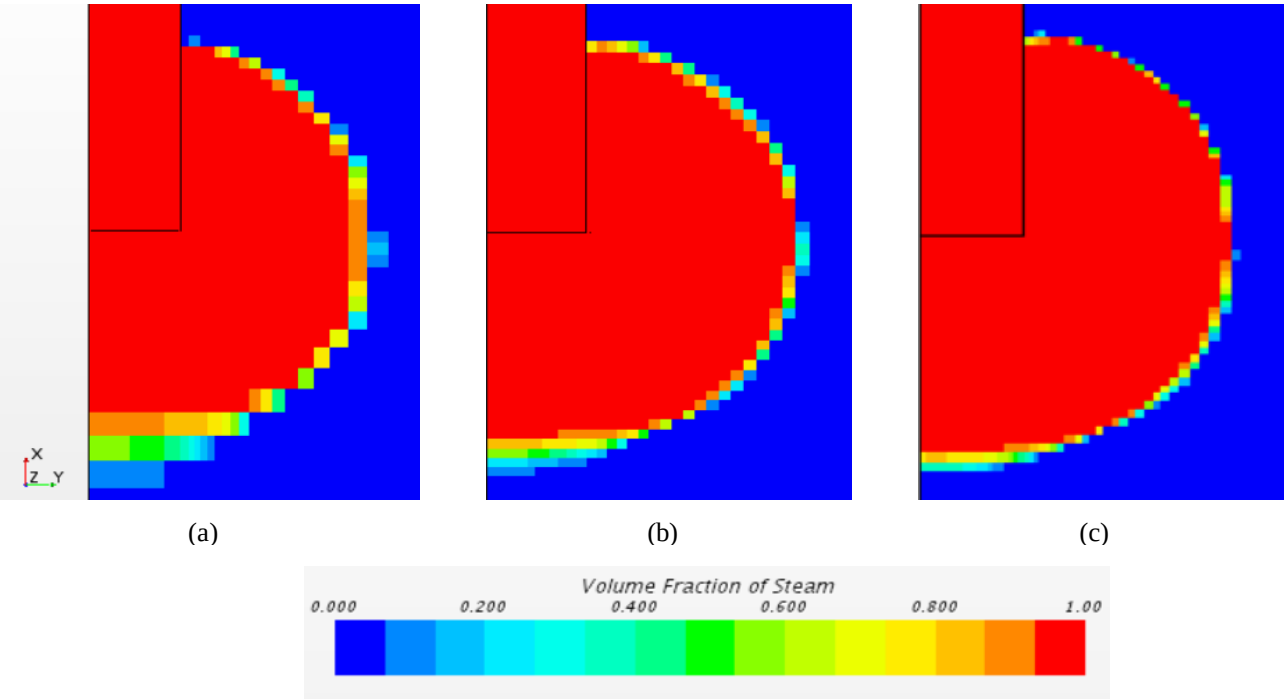

Figure 17. Steam Volume Fraction near t = 18.6 ms for (a) Grid C (b) Grid D (c) Grid E

From Figure 17, it is shown that the steam-water interface is captured at greater resolution as the mesh resolution increases. For Grid C, however, it is notable that there is substantial smearing in the interface which is characterized by lower gradients of the steam volume fraction in cells near the furthest extents of the bubble. Grids D and E give a much smoother steam-water interface with less interface smearing, thus providing a higher gradient of the steam volume fraction in cells at the furthest bubble extent.

The most dominant contribution to the total condensation rate in the Pool region comes from cells with the highest steam volume fraction gradient. Thus, with a large amount of interface smearing, the condensation rate is lowered as the interfacial area density, as defined in Equation 5.16, is lower under these conditions.

Therefore, the low magnitude of the condensation rate for the coarsest grid is explained, but the higher than expected interfacial area for Grid C requires more explanation. To assess this behavior, the penetration depth of the bubble for each grid was considered. Table 17 shows this result.

Table 17. Bubble Penetration Depth for Grids C, D, and E

Simulation Grid	**Penetration Depth (cm)**	**Time (ms)**
C	6.6	18.6
D	5.6	18.0
E	5.1	19.0

As shown in Table 17, the penetration depth of the bubble for Grid C is 25.6 percent higher than Grid E. Thus, Grid C exhibits steam penetration further into the Pool which contributes to having a higher total interfacial area. With a higher penetration depth and significant interface

smearing, the total interfacial area for Grid C can be higher while still having a much lower condensation rate.

Ultimately, Grid D and E have similar bubble penetration depth and total interfacial area. The interfacial area for Grid D is higher than Grid E, but the condensation rate for Grid E is higher. This is similar behavior as seen when comparing Grid C to the other grids, but the difference is much less severe. The reduced degree of smearing in the interface for the nominal and fine grid sizes makes both of these grids much more suitable for use than Grid C.

The percent difference in quantities of interest between the most refined mesh, Grid E, and the nominal refinement, Grid D, is within 10% on all quantities of interest. In the work by Pellegrini et al., increased grid refinement gave a similar percent difference in interfacial area between fine and nominal grid refinement [17] with the nominal grid being used in their final analyses.

9.1.3 Final Grid Selection

With Grid C being deemed unacceptable for further analysis, due to a high degree of smearing in the interface, Grids D and E were considered the best candidates for further analyses.

At this point in the grid comparison, it was decided that Grid D with 2-3 mm cell size in the refined portion of the Pool region would be used for further analysis. Using the nominal grid led to slightly faster run times than Grid E while only presenting a small disadvantage in performance with slightly greater interface smearing.

9.2 NHTS Test Case #4 Full Simulation Results

Having completed the grid convergence study, the simulation using Grid D was assessed to gain insights into the bubble formation and deformation process. The full simulation was carried out for a duration of 48 ms. This allowed for the ability to observe how the deformation of the bubble compares to behavior consistent with direct contact condensation flow regimes.

Figures 18-25 show the progression of the steam flow into the Pool by looking at steam volume fraction.

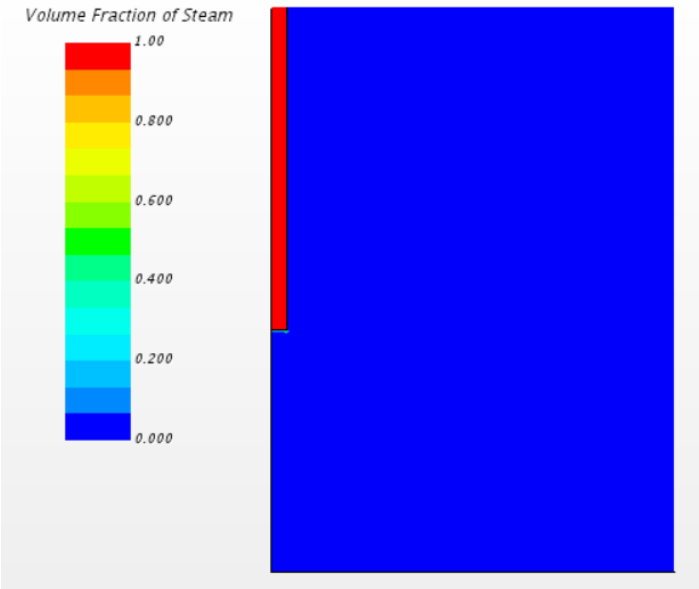

Figure 18. Steam Volume Fraction – 1 ms

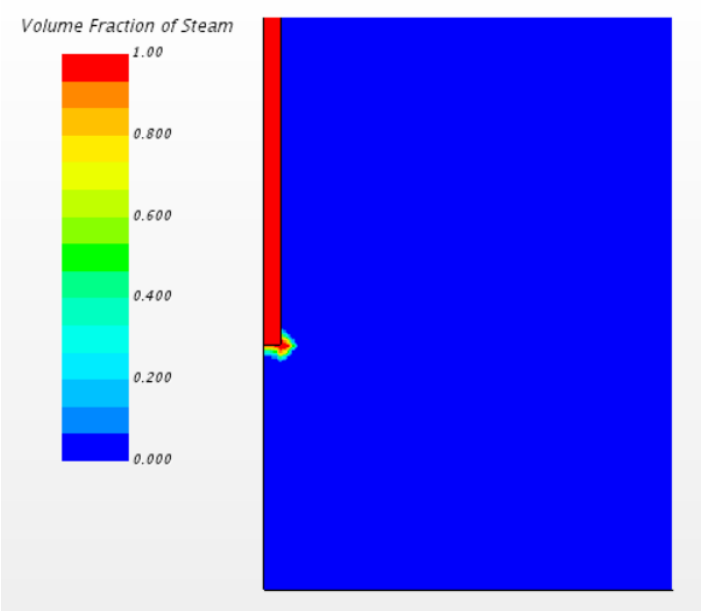

Figure 19. Steam Volume Fraction – 5 ms

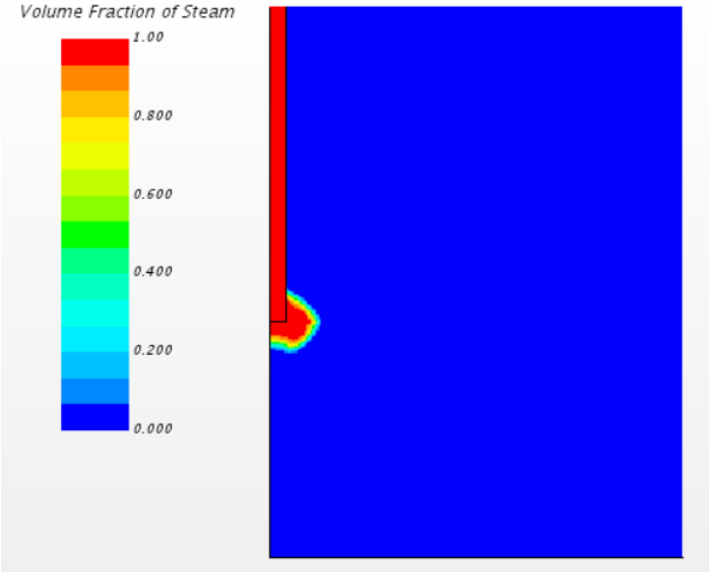

Figure 20. Steam Volume Fraction – 10 ms

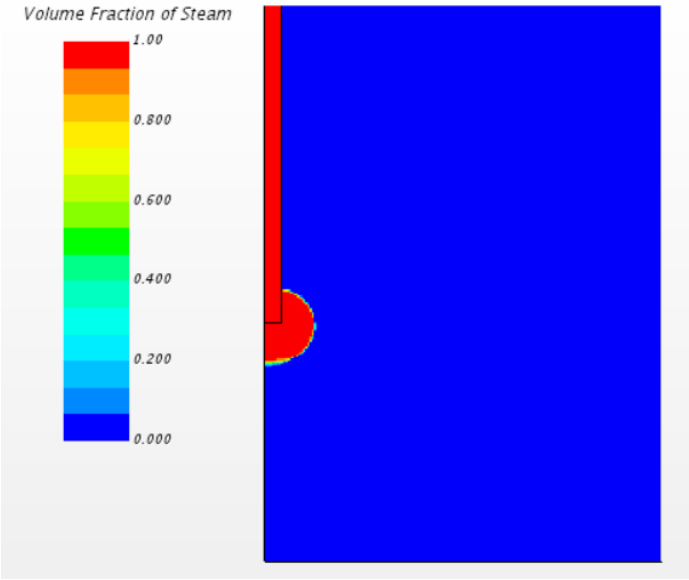

Figure 21. Steam Volume Fraction – 18 ms

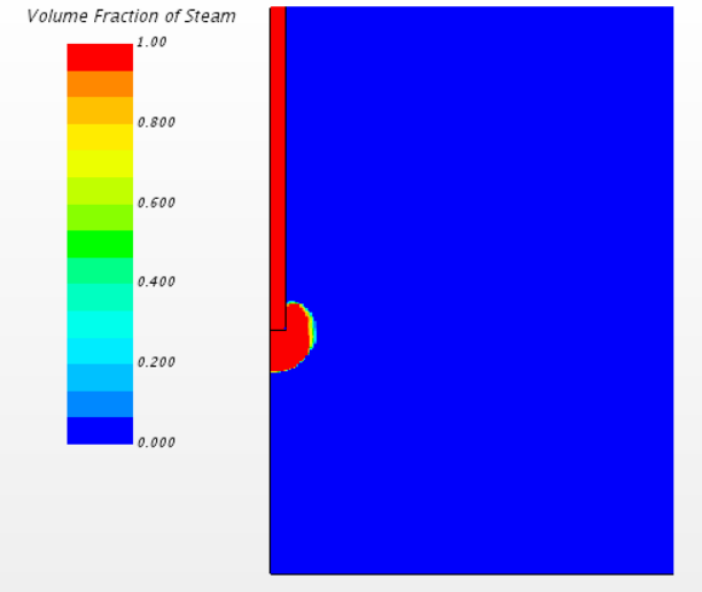

Figure 22. Steam Volume Fraction – 23 ms

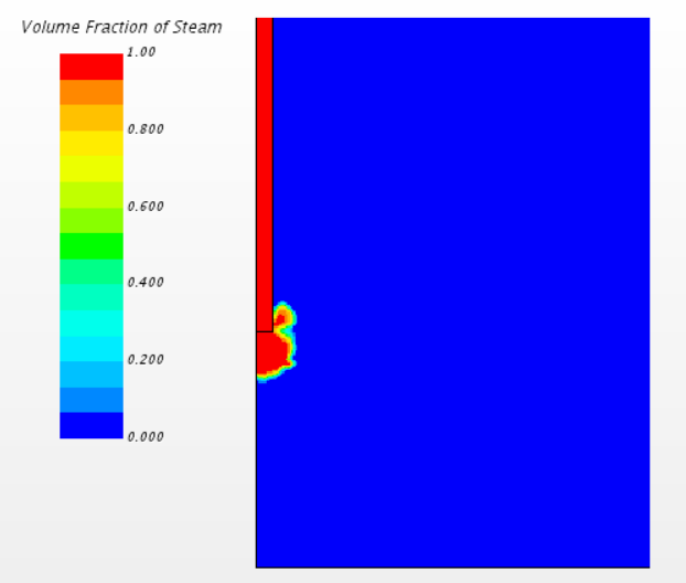

Figure 23. Steam Volume Fraction – 30 ms

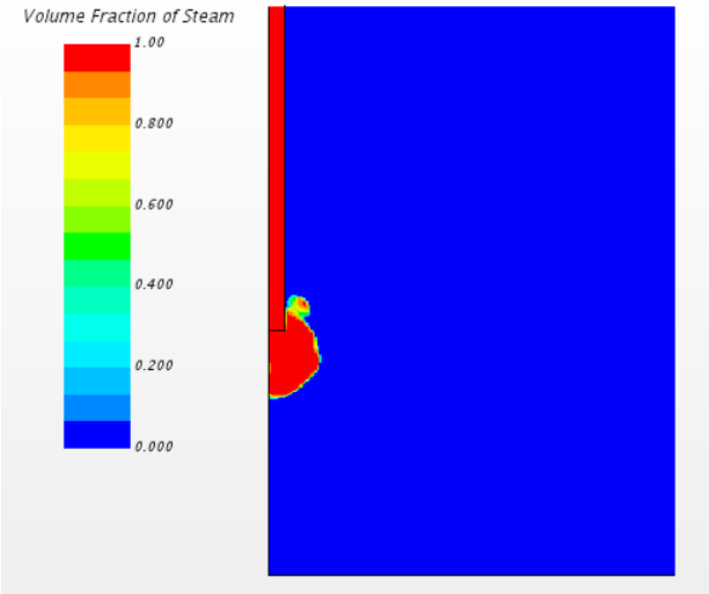

Figure 24. Steam Volume Fraction – 41 ms

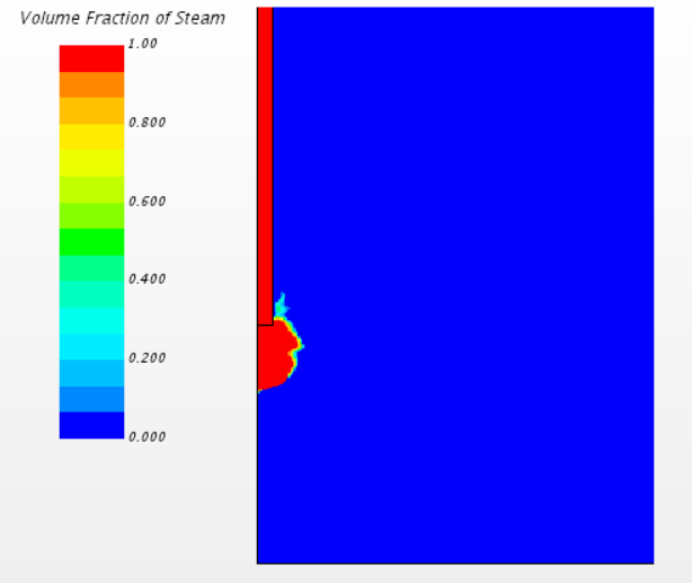

Figure 25. Steam Volume Fraction – 48 ms

As shown in Figure 20 and Figure 21, the bubble approaches its fullest extent between t = 10 ms and t = 18 ms. At 18 ms, the condensation rate reached 41.7 g/s which is just under the 45 g/s mass flow rate of steam into the Sparger. By t = 19.3 ms, the condensation rate reached 45.3 g/s, just exceeding the inlet mass flow rate of steam to the Sparger. It is at this point that steam begins condensing rapidly along the side of the bubble.

Figure 21 and Figure 22 show this progression from t = 18 ms to t = 23 ms. At t = 30 ms, the first bubble deformation reaches a final state with a pocket of the original steam bubble being ejected towards the pressure boundary. At this point, there is still a substantial amount of the core of the bubble still intact below the Sparger outlet. This was unexpected since it was thought that chugging would be the flow regime of direct contact condensation present given the initial Pool subcooling and steam mass flux which would lead to a full collapse of the bubble inward from the steam-water interface.

Between t = 30 ms and t = 48 ms, core region of the bubble below the Sparger outlet undergoes further growth. It is during this same time that the ejected portion of the bubble above the Sparger outlet began to itself collapse due to condensation as shown in Figure 24 and Figure 25. This leaves the bubble in a final state shown in Figure 25 where the bubble is now enlarged from its state at t = 18 ms with only minor remnants of the ejected steam pocket present above the Sparger outlet.

9.2.1 Quantitative Assessment of Bubble Evolution

Figure 26 and Figure 27 shed some light on bubble dynamics observed up to 48 ms.

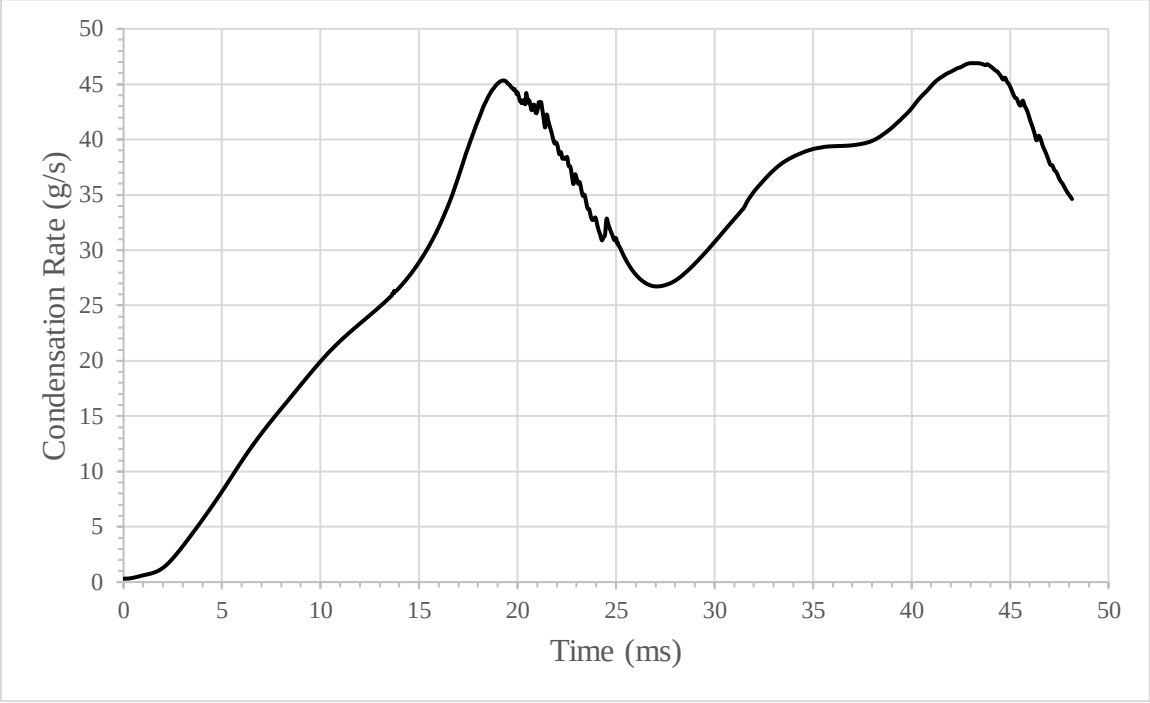

Figure 26. Condensation Mass Flow Rate for 48 ms of Time

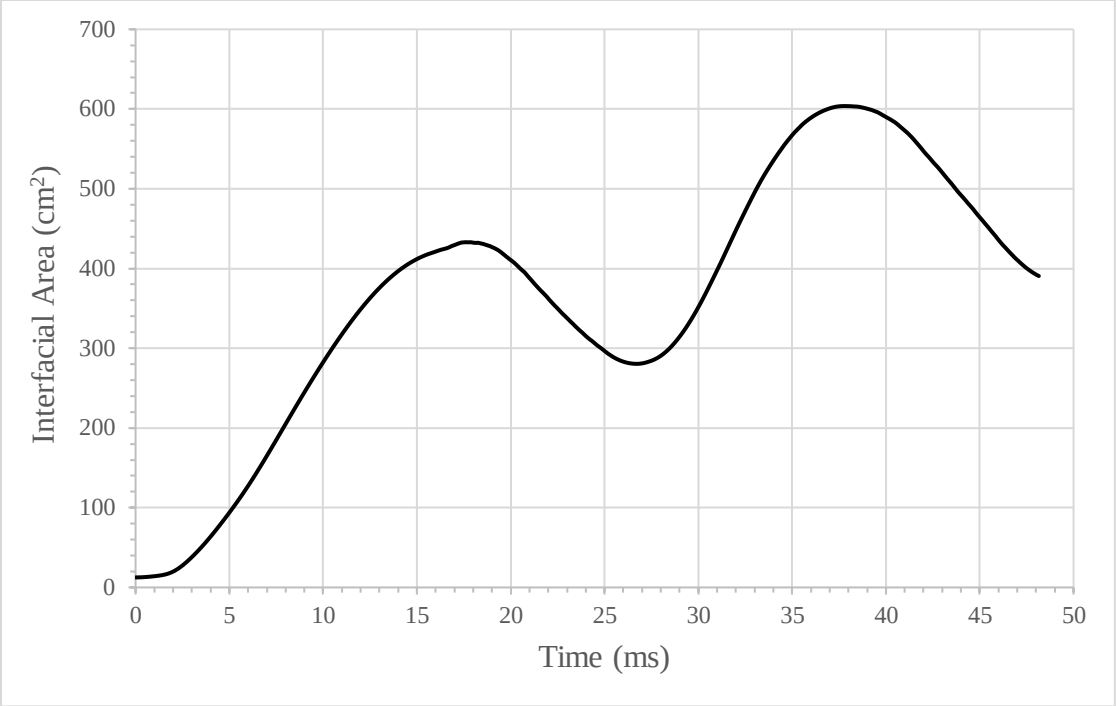

Figure 27. Bubble Interfacial Area for 48 ms of Time

From Figures 26 and 27, the bubble formation and deformation can be separated into the following phases:

- t = 0 – 5 ms : Over-pressurization in Sparger with bubble beginning to form in Pool.
- t = 5 ms – 18 ms : Under-pressurization in bubble and Sparger with bubble reaching fullest extents within the Pool.
- t = 18 ms – 20 ms : Maximum condensation rate achieved in the Pool.
- t = 20 ms – 28 ms : Bubble deforms collapsing inwards along the -y direction.
- t = 28 ms – 40 ms : Two steam pockets form. One pocket above the Sparger outlet rises slightly towards the pressure outlet boundary, but its flow towards the boundary is

significantly limited by condensation. The core bubble below the Sparger outlet begins to grow again.

- t = 40 ms – 48 ms : Steam pocket above Sparger outlet exhibits near complete condensation leaving only a core bubble volume in the Pool below the Sparger outlet.

Initially, the pressure within the Sparger rises significantly above the 197 kPa initial steam pressure as the steam mass flow rate at the Sparger exit is much lower than the steam mass flow rate into the Sparger. This occurs due to the need to displace water from the mouth of the Sparger to begin bubble formation in the Pool. Thus, up to 5 ms into the transient, pressure rises much higher than its initial condition which is shown in Figure 28. During this phase, a steam bubble begins forming in the Pool with the condensation rate and interfacial area increasing as shown in Figure 26 and Figure 27.

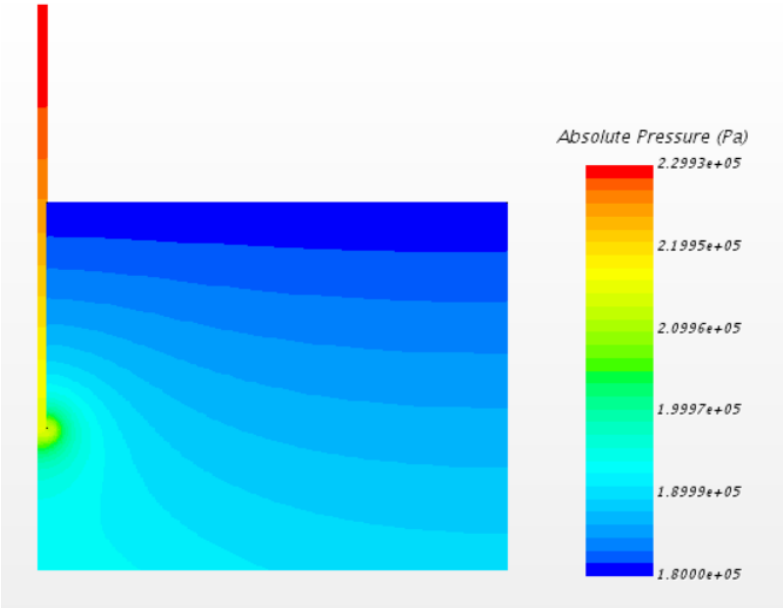

Figure 28. Over-Pressurization at t = 5 ms

Since the over-pressurization phase has created a high pressure gradient inside of the Sparger between the inlet and outlet, steam accelerates from the mass flow inlet boundary to the Sparger outlet. Over time, as a substantial steam flow is established into the bubble inside the Pool, the initial increase in pressure within the Sparger is reverted back towards and even reaches values below the initial pressure of 197 kPa. This is caused by the fact that steam mass flow rate exiting the Sparger will briefly exceed the steam mass flow rate into the Sparger. Figure 29 shows that this pressure drop is quite severe with absolute pressure dropping to near 40 kPa below the initial pressure inside of the Sparger. During the under-pressurization phase, the condensation rate and interfacial area continue to increase as the bubble volume increases towards its maximum value.

The severity of the pressure drop inside of the Sparger and bubble volume with the Pool has also been seen in literature, particularly in the case of the first bubble formation. As noted by Timperi et al., measured pressures at the Sparger outlet of the POOLEX facility decrease as the first bubble is formed [24]. However, as the bubble begins to collapse, water flow towards the Sparger outlet leads to an overall increase in pressure. Finally, as a new steam water interface is created near the Sparger outlet, the process starts over again. However, it must be noted that in [24] the magnitudes of the over-pressurization and under-pressurization events are less for subsequent bubble formations.

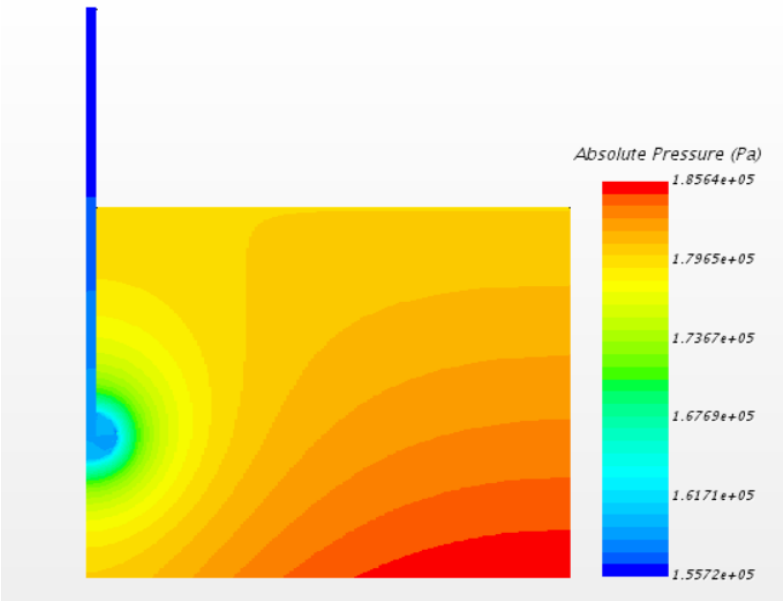

Figure 29. Under-Pressurization at t = 18 ms

The large under-pressurization that takes place in the Sparger and bubble creates an unfavorable condition for continued bubble growth with the condensation rate approaching a maximum value. As noted previously, at t = 19.3 ms, the condensation rate reaches a peak of 45.3 g/s. The high condensation rate, in conjunction with the pressure gradient aligned towards the core of the bubble, causes the bubble to begin to deform.

From Figure 26 and 27, during the deformation phase from t = 20 ms to 28 ms, the interfacial area decreases as the bubble begins to collapse. This is intuitively accompanied by a decrease in the condensation rate. It is during this phase that it becomes clear that the chugging direct contact condensation flow regime is not present, with the bubble deforming most severely along a path in the -y direction towards the Sparger outlet.

At approximately t = 30 ms, it was previously noted that there were two clear steam pockets remaining after the deformation occurred. From t = 28 ms to 40 ms, the core bubble below the

Sparger begins to exhibit further growth. Since the core bubble exhibited incomplete condensation in the first bubble deformation phase, this bubble is able to reach even further physical extents within the Pool region than achieved during the first bubble formation phase. The bubble pocket above the Sparger outlet, rises slightly towards the pressure boundary, but its progress is limited by condensation in the Pool. Thus, the interfacial area and condensation rate begin to increase during this phase of bubble reformation with the most significant contribution to this increase coming from the core bubble below the Sparger.

Finally, at t = 40 ms, the bubble has reached its maximum interfacial area and the condensation rate has reached a value of 46.8 g/s. The bubble begins a second deformation phase that has two consequences. First, the ejected bubble pocket above the Sparger collapses due to a high rate of condensation taking place. Next, the core bubble starts to collapse again in the -y direction. Thus, interfacial area and condensation rate decrease during this phase.

9.2.2 – Assessment of Direct Contact Condensation Flow Regime

Overall, the principle question that arises from this simulation is why the bubble did not fully collapse. This is explained by assessing the rate of condensation taking place. Figure 30 shows the interaction area density at t = 18 ms while Figure 31 shows the condensation rate per unit volume.

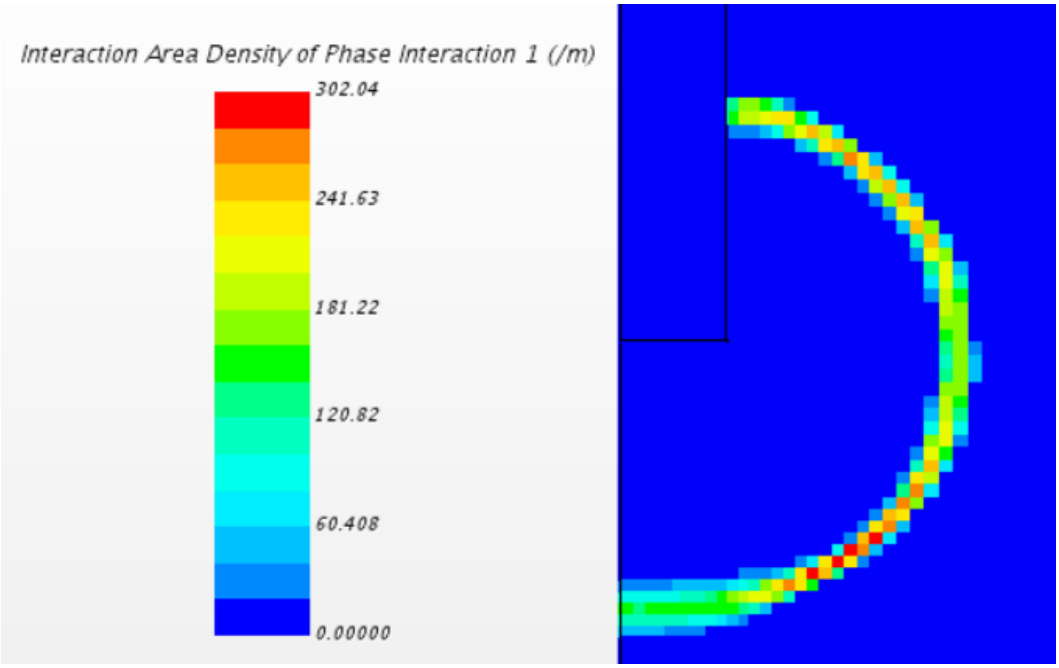

Figure 30. Interaction Area Density at t = 18 ms

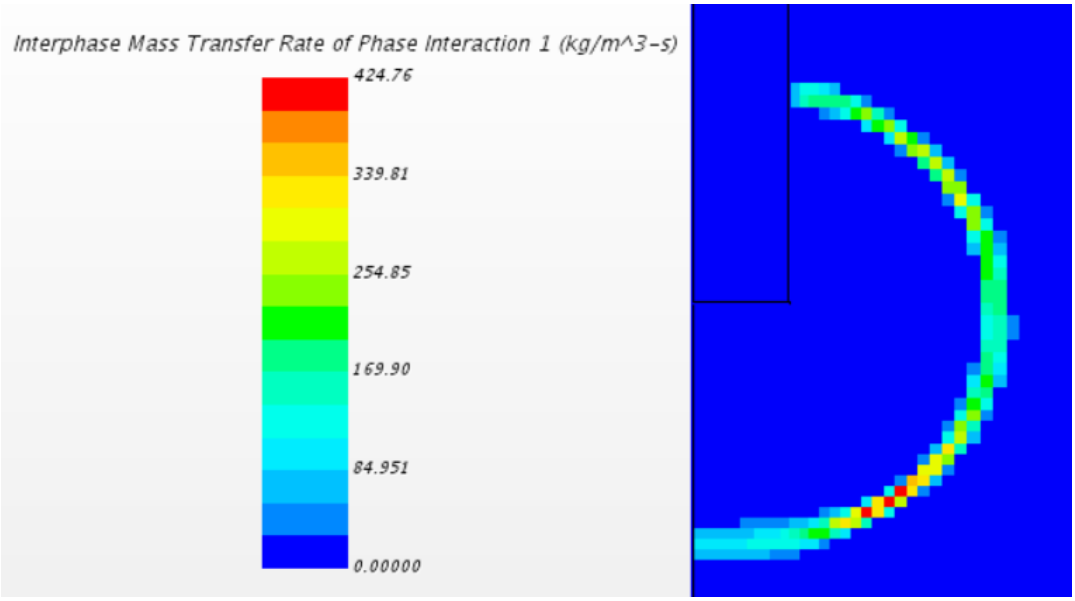

Figure 31. Condensation Rate per Unit Volume at t = 18 ms

Figure 30 and Figure 31 show that condensation is occurring near the periphery of the bubble as expected where the interaction area density is non-zero at the steam-water interface. However, it is also important to assess the magnitude of the condensation rate. In Figure 26, the condensation mass flow rate is shown to rise up to 45.3 g/s which is below the inlet steam mass flow rate of 45 g/s. While this magnitude of condensation taking place is higher than the inlet steam mass flow rate, it is not sufficiently high enough to observe the chugging direct contact condensation flow regime.

Therefore, the flow regime observed in this simulation was more consistent with the bubbling regime. In the bubbling regime, as depicted by de With et al. in [8], the bubble grows to its maximum radius and begins deforming with the overall deformation appearing similar to necking occurring for a steam bubble beginning to detach from a solid surface. The bubble can detach from the Sparger with a new bubble subsequently beginning to form. In this simulation the bubble deformation did not yield complete detachment from the Sparger outlet. However, there is evident instability in the bubble (both at t = 30 ms and t = 48 ms) that is shown by both the steam volume fraction profiles and the reductions in steam interfacial area.

The condensation rate was high enough after the regrowth phase (starting after t = 30 ms) to cause the steam pocket above the Sparger outlet to exhibit near complete condensation. By t = 48 ms, the core bubble was beginning to undergo a second deformation phase along the -y direction as shown in Figure 25 indicating that the deformation of the bubble will exhibit a periodic behavior which occurs in both bubbling and chugging flow regimes.

Therefore, since the observed direct contact condensation flow regime was not consistent with chugging, other phenomena of interest must have a significant effect on the condensation rate achievable in the system. As discussed in Section 3, Rayleigh-Taylor instability is expected to be

prevalent in these steam-water Suppression Chamber systems. The effect of Rayleigh-Taylor instability is to accelerate the increase in total available interfacial area for mass transfer over time. As shown in Equation 3.2, the wave amplitude for Rayleigh-Taylor instability increases exponentially with time which ultimately, later in the bubble formation process, leads to similar exponential growth in the available interfacial area.

Thus, implementation of a Rayleigh-Taylor instability model as in [17] would have two effects on the results of this simulation. First, the condensation rate would be increased substantially leading to a condition where the condensation rate is much greater than the inlet mass flow rate of steam. This would induce the chugging DCC flow regime to take place rather than a condition most similar to bubbling as seen in this simulation. Next, implementing a Rayleigh-Taylor instability model would lead to much smaller bubble sizes than seen in this simulation. This is also directly tied to the fact that the exponentially increasing magnitude of the condensation rate would counteract the rate of bubble growth. Preliminary simulations utilizing the Rayleigh-Taylor instability model to correct the interfacial area density did exhibit this exponential increase in interfacial area, but convergence issues made it unsuitable for presentation in the current work.

According to direct contact condensation flow regime maps, such as those from de With et al., the conditions simulated here for Test Case #4 should fall in the chugging DCC flow regime. However, while conducting the Test Case #4 experiment, it was observed that under these average water temperature and vapor space pressure conditions, audible chugging events were becoming less noticeable [7]. To explain this behavior, the role of axial water temperature stratification in the Pool should be considered. While only weak axial Pool temperature stratification existed when considering the entire Pool volume at large under the conditions

simulated in this work, it is very likely that water temperatures closer to the Sparger outlet were substantially warmer in comparison to other axial regions of the Pool. This would cause a much lower degree of subcooling to exist in the axial regions that contain the bubble volume which would induce the bubbling DCC regime.

Unfortunately, it is not possible to ascertain the physical extent of the location of a local hot spot near the Sparger outlet in Test Case #4. However, one thermocouple in the experiment was located near outlet of the Sparger. Temperature readings at this location near the outlet are shown below in Figure 32.

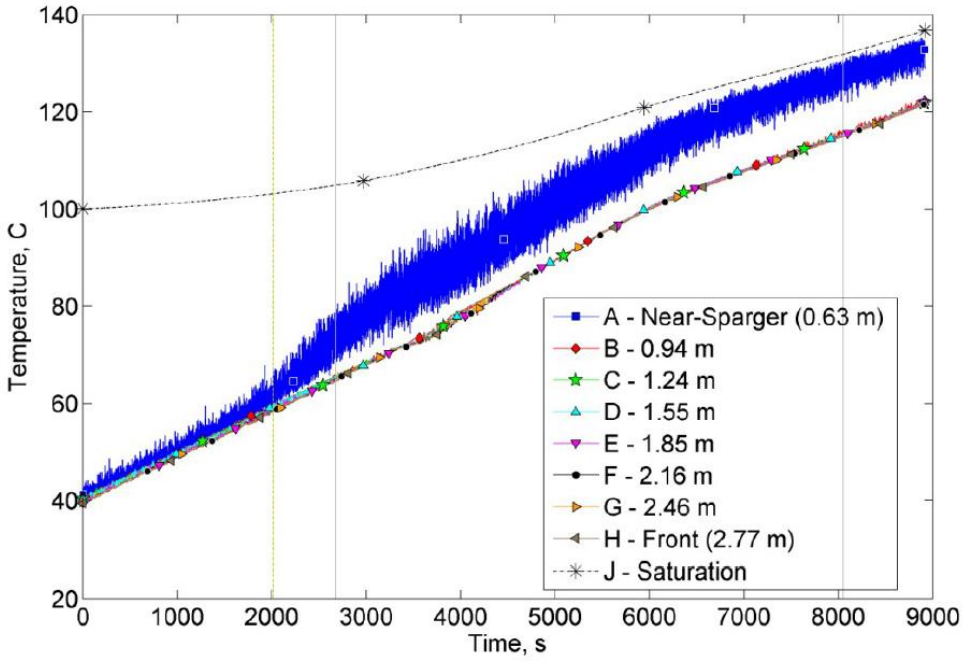

Figure 32. Water Temperature Near Sparger for Test Case #4 [7]

In Figure 32, it is shown that temperature readings near the Sparger outlet at t = 4000 s (the time where the average conditions of the simulation were present) are over 10 °C higher than the water temperature initialization in the Pool for this simulation which would move the projected DCC flow regime within the bubbling regime. However, if more thermocouples were placed within a 10 cm radius of the Sparger outlet, the extent of this local hot spot could be more well characterized.

Finally, it must also be noted that this simulation assumed that the Chamber vapor space was not vented with the pressure boundary set to 180 kPa, much higher than atmospheric pressure. In the work by Solom in [11], it is noted that pressurization in the Chamber led to increased temperature stratification in the Pool which is characteristic of the bubbling flow regime being present.

Therefore, the resulting direct contact condensation flow regime of this simulation may have been greatly impacted by the selection of a high pressure at the Pool surface. The depressive effect of Chamber pressurization on Pool mixing should be considered in future work by considering other Chamber pressures in setting the pressure boundary condition.

9.3 Insights to Experimental Design of NHTS Facility

One of the principle objectives of this work is to identify experimental design changes that can be made at the NHTS facility to provide the ability to validate CFD models of short transients with direct contact condensation conditions present.

In this work, a few issues were identified based on the results of the simulations:

- Time resolution of pressure measurements

- Location of pressure measurements
- Spatial resolution of temperature measurements near the Sparger outlet

At the NHTS facility, all instrument measurements were taken at a frequency of 10 Hz. One differential pressure measurement is taken between the Sparger inlet and the Chamber vapor space.

Based on the CFD simulations, it is observed that significant pressure transients take place much faster than this measurement frequency of 10 Hz with the over-pressurization phase taking place over 5 ms and the under-pressurization phase taking place on the order of 10 ms. Furthermore, the location of interest for a pressure measurement to take place is near the Sparger outlet, which can only be extracted indirectly from the differential pressure readings that are currently available.

Within the Pool, there are thermocouples spread both horizontally and vertically which allowed for the assessment of temperature stratification in the Pool over a long transient. A diagram of the thermocouple placements was developed by Solom in [7] and is shown in Figure 6.

From Figure 6, it is shown that there is one thermocouple located just outside Sparger outlet and one thermocouple just inside the Sparger. However, these two thermocouples are not sufficient to obtain a representative profile of a possible hot spot in the Pool near the Sparger. Based on the simulation results in this work, it is recommended that more spatial resolution in temperature be obtained near the Sparger outlet where the bubble forms and deforms over time since the water temperature in this region has a significant effect on the observed direct contact condensation flow regime.

From the simulation in this work, it is also notable that a portion of the steam bubble exist above the Sparger outlet. It was also observed that at this location there is a likelihood of a separation taking place forming separate steam pockets above and below the Sparger after the bubble undergoes deformation. However, there are no thermocouples present within 5 cm vertically from the Sparger outlet towards the Pool surface.

Thus, based on this assessment of the NHTS facility with respect to the simulation results, the following recommendations are provided:

- Increase pressure measurement frequency to 500-1000 Hz for new pressure sensors.
- Add an additional absolute pressure transducer near the Sparger outlet to be near the location of interest for bubble dynamics.
- Add thermocouple locations closer to the Sparger outlet (both below the Sparger and above the Sparger towards the Pool surface)

The addition of thermocouple locations near the Sparger likely presents the greatest challenge for experimentalist at the NHTS facility since these locations would require a structure to hold them in place. From the simulation in this work, the bubble penetration depth before the first deformation was 5.6 cm. While it would be preferable to have multiple thermocouples within the core volume of the steam bubble, it is acknowledged that this may be difficult to achieve with existing structure in the Pool. It is also acknowledged that adding support structure within this region could affect the dynamics of the bubble formation. Therefore, from this work it is recommended that 1-2 thermocouples be placed within 10 cm of the Sparger outlet. Even if the thermocouples are located outside of the core volume of the bubble, these thermocouples could provide context to the extents that a hot spot may exist.

9.4 Best Practices for Eulerian Multiphase Simulations

Based on these results, there are a few best practice guidelines that helped in leading to successful simulations. These best practice guidelines are listed below.

- In order to aid convergence during periods where complex flow and condensation behaviors are exhibited, lowering under-relaxation factors can help prevent solution divergence. Under-relaxation factors for the Eulerian multiphase segregated flow model that were found to be most impactful were for volume fraction and energy. However, it is important to note that lowering under-relaxation factors too severely will slow down the convergence leading to the need for many inner solver iterations per time step.
- During the initial over-pressurization and under-pressurization phases of the simulations in this work, the steam temperature can anomalously rise in regions of the domain where steam is only present at the minimum volume fraction. It was found that after the under-pressurization phase, steam temperatures in these regions returned to a more normal status. One way to prevent this from occurring is to utilize the maximum temperature limit in the STAR-CCM+ reference parameter tab. By setting this maximum temperature to the initial temperature of steam in the Sparger region, it is possible to prevent the anomalous behavior, and later in the simulation the maximum temperature limit can be increased without any issues.
- Convergence in simulation using the Eulerian multiphase segregated flow model should be assessed from multiple perspectives. During certain periods of the simulation, energy residuals can be difficult to converge to a value below 1E-4. However, it is possible to assess convergence based on other field parameters such as condensation rate which in this work was a major influence on flow behavior. By observing convergence of this

parameter to a proscribed tolerance of 1% inlet mass flow rate over all inner iterations of a time-step, it was deemed acceptable to relax tolerances on certain RMS residuals.

- Particular care should be taken in defining the interaction length scale in these simulations. This length scale has impacts on many parameters including drag force and mass transfer rate.
- Implementation of IAPWS steam and water tables within STAR-CCM+ gives the benefit of having a more realistic phase interface temperature especially during pressure transients that take place within the system. There is also the added benefit that the latent heat of vaporization at the phase interface is calculated internally from the tables which allows the user the ability to forgo use of manually generated internal tables to calculate this parameter.
- Both mass flow inlet and velocity inlet boundary conditions can be employed at the for steam at the Sparger inlet. However, noticeable variation in the steam mass flux entering the domain was observed for the velocity inlet during periods where a large pressure transient occurs (due to the effect of system pressure on steam density calculation from the steam table). The mass flow inlet boundary condition, which is typically used for highly compressible flows, was found to be suitable for use in this simulation and was able to maintain a constant mass flux of steam into the domain boundary. For experiments that hold steam mass flux constant, the mass flow inlet boundary condition would be more realistic.

10. CONCLUSIONS

This work considers the Pressure Suppression Chamber, a component of the Reactor Core Isolation Cooling System that is instrumental in maintaining core cooling capabilities during conditions such as the station blackout that occurred at Fukushima Daiichi. In previous experimental work at the NHTS Suppression Chamber facility, bulk pool temperature stratification was assessed during long term transients consistent with conditions at Fukushima. In this work, short-term mixing behavior in the NHTS Suppression Chamber system is assessed using computational fluid dynamics.

In this work, direct contact condensation was modeled within the STAR-CCM+ code utilizing experimental conditions from Test Case #4 at the NHTS Suppression Chamber experimental facility. The 2D axisymmetric formulation of the Eulerian multiphase segregated flow model was employed with the condensation modelled utilizing the Hughes-Duffey Nusselt number correlation. Steam and water properties were computed using built in IAPWS water and steam tables in STAR-CCM+. The resulting flow induced by the condensation phenomena was assessed.

Through a grid convergence study, a 2D axisymmetric structured mesh was found to be the best candidate for use in calculations in this work. Using a cell size gradient of 2-3 mm in a refined region around the Sparger, the resulting condensation rate, bubble interfacial area, and bubble penetration depth were found to be within 10% of values obtained using a similar 2D axisymmetric mesh with 1-2 mm cell size in the refined region of the Pool. A polyhedral mesh formulation was also assessed and was found to be inadequate for the current work due to issues in convergence particularly related to turbulence quantities.

Using conditions from Test Case #4 of the NHTS facility for initial and boundary conditions of this model, it was found that the dynamics of the initial steam bubble formation can be separated into an over-pressurization phase and under-pressurization phase. It is during the under-pressurization phase that condensation mass transfer begins to limit further growth of the bubble, eventually leading to a clear deformation of the steam bubble. It was observed that pressure within the Sparger increased near 30 kPa above the initialized steam pressure of 197 kPa followed by a large decrease in pressure 40 kPa below the initialized pressure.

The severity of the deformation of the steam bubble was found to be directly related to the condensation rate in the system. In this work, it was found that the maximum achieved condensation rate of 45.3 g/s was much too low to result in the expected chugging direct contact condensation flow regime given the initial subcooling in the system, but clear evidence supports that the condensation rate was indeed high enough to result in flow behavior most consistent with the bubbling DCC flow regime. In this work, it was observed that while the deformation did not lead to complete bubble collapse consistent with the chugging DCC flow regime, there was significant deformation of the bubble that led to the formation to two steam pockets above and below the Sparger. The resultant steam volume above the Sparger exhibited near complete condensation by the end of the simulation while the steam volume below the Sparger underwent a regrowth phase before starting a second deformation phase.

Experimentally at the NHTS facility, the bubbling DCC flow regime does appear to begin taking place at the vapor space pressure and average Pool temperature that were simulated in this work. However, it is possible that the observed DCC flow regime in the experiment is induced by a local hot spot existing near the Sparger outlet which was not captured in this work.

The observed flow regime in this work gives ample support for the necessity of capturing Rayleigh-Taylor instability in Suppression Chamber systems. Rayleigh-Taylor instability increases the available interfacial area for condensation leading to higher condensation rates and the capability of producing a chugging event.

Finally, it is notable that the choice of a high Pool surface pressure boundary condition (to mimic the pressurization of the Chamber over the time of the test) may have greatly impacted the observed flow regime in the simulations. Experimentally, Chamber pressurization led to greater temperature stratification in the Pool. Therefore, it is anticipated that a pressurized Chamber had a depressive effect on Pool mixing in these simulations.

Given these conclusions from the current work, the following goals were met:

- A simplified CAD geometry of the NHTS facility was generated and the Eulerian multiphase segregated flow model was implemented with the 2D axisymmetric formulation.
- IAPWS steam and water tables were successfully implemented for use in computing steam and water properties during simulation. This allows for more realistic setting of the phase interface temperature during significant pressure transients when compared to a constant phase interface temperature setting.
- Utilizing a mass flow inlet boundary at the Sparger inlet for simulation, a constant steam mass flux into the system was able to maintained as was done during the experiments which was found to be difficult to achieve with a velocity inlet boundary condition due to variation in density caused by large pressure variations that exist during steam bubble formation and collapse.

- Using average Suppression Chamber conditions during an experimental test case at the NHTS facility, the capability of the CFD model to capture direct contact condensation flow regimes was successfully assessed. Conditions most consistent with the bubbling regime were exhibited within the simulation. The chugging flow regime was not able to be captured due to an insufficient condensation rate in the system under these conditions.
- Insights into experimental design of the NHTS facility were made. The need for higher frequency pressure instrumentation (500-1000 Hz) was identified as critical for future model validation work. Furthermore, the possibility of adding more thermocouples closer to the Sparger outlet was identified as critical for setting a more realistic water temperature initial condition for future simulations.

10.1 Future Work

As shown in this work, the observed bubbling direct contact condensation flow regime conformed with the flow regime exhibited under the same experimental flow conditions. However, the reason for observing this flow regime in the simulation were due to an insufficient condensation rate taking place at the initialized Pool subcooling. In actuality, the presence of a local hot spot near the Sparger outlet most likely explains the presence of the bubbling DCC flow regime in the experiment.

Therefore, for future CFD work the following steps are proposed:

- Initialization of the Pool water temperatures to reflect stratified conditions in order to observe the bubbling DCC flow regime under more realistic conditions.

- Simulations performed with even greater subcooling and lower pressurization in the Suppression Chamber vapor space. These simulations would have conditions that induce the chugging DCC flow regime.
- Implementation of a Rayleigh-Taylor instability model as done in [17]. This should cause a clear chugging DCC flow regime to take effect in the system when conditions allow for this regime to initiate.

For future experimental work, the following recommendations are made based on the results of this work:

- Introduction of more thermocouples inside the Sparger to track the progression of a chugging event as water reverses back into the Sparger.
- Utilization of higher frequency pressure instrumentation. The formation and collapse of a bubble in the system has critical phases that occur faster than the instrumentation frequency of 10 Hz which makes CFD model validation difficult.
- Possible implementation of more thermocouples closer to the region of bubble formation at the Sparger outlet would provide data that allows improved initial conditions for water temperature.

REFERENCES

[1] R. O. Gauntt, "RCIC Operation in Fukushima Accidents as Modeled by MELCOR and Proposed Testing," Sandia National Laboratories, 7 October 2014. [Online]. Available: https://inis.iaea.org/collection/NCLCollectionStore/_Public/47/066/47066815.pdf.

[2] U. N. R. Commission, "Boiling Water Reactor (BWR) Systems," 2019.

[3] U. N. R. Commission, "Reactor Core Isolation Cooling Reliability Study," November 2005. [Online]. Available: nrcoe.inl.gov/resultsdb/publicdocs/SystemStudies/rcic-system-description.pdf..

[4] T. E. P. Company, "The Cause of RCIC Shutdown in Unit 3," 2014. [Online]. Available: www.tepco.co.jp/en/press/corpcom/release/betu17_e/images/171225e0237.pdf..

[5] G. Electric, "Mark I Containment Report," March 2011. [Online]. Available: files.gereports.com/wp-content/uploads/2011/10/NEI-Mark-1-White-Paper.pdf.

[6] T. E. P. Company, "Schematic Drawing of Unit 2 RCIC Turbine Exhaust Pipe," October 2013. [Online]. Available: fdada.info/docdata/accident_analysis/Unit2_RCIC-quencher.pdf..

[7] M. Solom, "Experimental Study On Suppression Chamber Thermal-Hydraulic Behavior For Long-Term Reactor Core Isolation Cooling System Operation," Texas A&M University Libraries, 2016.

[8] A. de With, R. K. Calay, G. de With and A. E. Holdo, "Regimes of Direct Contact Condensation of Steam Injected into Water," *The International Journal of Multiphysics*, vol. 1, no. 3, pp. 270-282, 2007.

[9] P. J. Kerney, "Penetration Characteristics of a Submerged Steam Jet," *AIChE Journal*, vol. 18, no. 3, pp. 548-553, 1972.

[10] H. Purhonen, M. Puustinen, J. Laine, A. Raesaenen, R. Kyrki-Rajamaeki and J. Vihavainen, "Steam blowdown experiments with the condensation pool test rig," in *Proceedings of the International Conference Nuclear Energy for New Europe*, Slovenia, 2005.

[11] M. Solom and K. V. Kirkland, "Experimental Investigation of BWR Suppression Pool Stratification During RCIC System Operation," *Nuclear Engineering and Design*, vol. 310, pp. 564-569, 2016.

[12] J. Laine and M. Puustinen, "Thermal Stratification experiments with the condensation pool test rig," Nordic Nuclear Safety Research (NKS), 2006.

[13] V. Tanskanen, "CFD modelling of direct contact condensation in suppression pools by applying condensation models of separated flow," LUTPub, 2012.

[14] ANSYS, *FLUENT 6.3 User's Guide,* 2006.

[15] M. Meier, G. Yadigaroglu and M. Andreani, "Numerical and Experimental Study of Large Steam-Air Bubbles Injected in a Water Pool," *Nuclear Science and Engineering,* vol. 136, no. 3, pp. 363-375, 2000.

[16] S. Li, "Numerical Simulation of Direct Contact Condensation of Subsonic Steam Injected in a Water Pool Using VOF Method and LES Turbulence Model," *Progress in Nuclear Engery,* vol. 78, pp. 201-215, 2015.

[17] M. Pellegrini, M. Naitoh, C. Josey and E. Baglietto, "Modeling of Rayleigh-Taylor Instability for Steam Direct Contact Condensation," in *The 16th International Topical Meeting on Nuclear Reactor Thermal Hydraulics (NURETH-16),* Chicago, IL, 2015.

[18] V. Tanskanen, "CFD Simulation and Pattern Recognition Analysis of the Chugging Condensation REgime," *Annals of Nuclear Energy,* vol. 66, pp. 133-143, 2014.

[19] L. Rayleigh, "Investigation of the Character of the Equilibrium of an Incompressible Heavy Fluid of Variable Density," in *Proceedings of The London Mathematical Society,* 1883.

[20] G. Patel, "Computational Fluid Dynamics Analysis of Steam Condensation in Nuclear Power Plant Applications," LUTPub, 2017.

[21] C. Josey and E. Baglietto, "Adding a Rayleigh-Taylor correction factor for the analsis of sparger operation," MIT, 2014.

[22] D. Livescu, "Compressibility effects on Rayleigh-Taylor instability growth between immiscible fluids," *Physics of Fluids,* vol. 16, no. 1, pp. 118-127, 2003.

[23] Siemens, *STAR-CCM+ Version 13.04.011-R8 User Guide,* 2018.

[24] A. Timperi, M. Chauhan, T. Pättikangas and J. Niemi, "Modeling of interaction of multiple vent pipes in a pressure suppression pool," Nordic Nuclear Safety Research, 2012.